Article:
Rund, Phil, Lee, Ben H., Moon, Allison R. et al. (2026) Observations of Reactive Bromine in the Sub-Tropical Marine Boundary Layer. American Chemical Society Environmental Science and Technology Air. 2111–2127. ISSN: 2837-1402

https://doi.org/10.1021/acsestair.6c00124

Observations of Reactive Bromine in the Sub-Tropical Marine Boundary Layer

Phil Rund[1], Ben H. Lee[1], Allison R. Moon[1], Becky Alexander[1], Siddharth Iyer[2], Gordon A. Novak[3], Andrew Rollins[3], Amy Lees[4], Jake T. Vallow[4], Lewis Marden[4], Lucy J. Carpenter[4], Mat J. Evans[4], Marvin D. Shaw[4,5], Pete M. Edwards[4], Alyson Fritzmann[6], Jochen Stutz[6], and Joel A. Thornton[1]

[1]Department of Atmospheric and Climate Science, University of Washington, Seattle, WA, 98195, U.S.A.

[2]Aerosol Physics Laboratory, Tampere University, Tampere, Pirkanmaa, FI

[3]NOAA Chemical Sciences Lab, Boulder, CO 80305, U.S.A.

[4]University of York, Wolfson Atmospheric Chemistry Laboratories, Department of Chemistry, York, United Kingdom

[5]National Centre for Atmospheric Science, United Kingdom

[6]University of California Los Angeles Department of Atmospheric and Oceanic Sciences, Los Angeles, CA, United States

Abstract

Reactive bromine species in the troposphere affect ozone (O_3) as well as the cycling and fate of hydrogen oxide HO_x and nitrogen oxide NO_x radicals, with implications for the oxidative capacity of the atmosphere, greenhouse gas budgets, air quality, and human health. However, uncertainties remain in the global distribution and chemical mechanism of inorganic bromine with few in-situ observations, especially outside of polar regions. We present results of speciated gas-phase reactive bromine observations made in the Marine Boundary Layer (MBL) at a coastal site in the Northwest Atlantic Ocean during January and February 2023, as part of the Bermuda boundary Layer Experiment on the Atmospheric Chemistry of Halogens (BLEACH)

campaign. Using an iodide-adduct High Resolution Time of Flight Chemical Ionization Mass Spectrometer (HR-ToF-CIMS) equipped with a custom atmospheric pressure transverse ion-molecule reaction region (t-IMR), we observe sub-ppt levels of atmospheric inorganic bromine compounds including Br_2, BrCl, HOBr, $BrONO_2$, and BrO in the marine boundary layer. To our knowledge, these are the first reported in-situ observations of gaseous bromine nitrate ($BrONO_2$). An experimental calibration for hypobromous acid (HOBr) produces sensitivity values in agreement with previous studies and theoretical calculations involving binding enthalpies, which we use to convert measured ion signals to units of ambient mixing ratios. We characterize the relationship between reactive bromine levels and surrounding environmental factors including meteorological conditions, influences from local pollution sources, and "clean marine" periods of onshore winds. Measured mixing ratios for all bromine species are found to be much lower than predicted by a GEOS-Chem model simulation which includes fully coupled reactive halogen chemistry. We discuss the implications of this discrepancy on reactive bromine sources and multi-phase chemistry.

1 Introduction

1.1 Reactive Halogens in the Troposphere

Atmospheric reactive halogen-containing species, defined here as compounds containing chlorine (Cl), bromine (Br), and iodine (I) atoms, influence the climate system and human health. Reactive halogens can greatly affect the oxidation capacity of atmosphere, air quality, and climate via a suite of direct and indirect pathways, and can catalytically destroy ozone (O_3) [1][2][3][4] Tropospheric ozone is an important greenhouse gas and a pollutant with adverse effects on plant, animal, and human health.[5] As the dominant global source of the hydroxyl radical, OH, processes that affect the tropospheric ozone burden indirectly affect oxidizing capacity and the lifetimes of reactive trace gases, including the greenhouse gas methane.[6] Halogen oxide radicals also react with HO_x (= OH + HO_2) to varying degrees, modulating both the concentrations and ratio of OH and HO_2, and therefore can have significant direct impacts on the oxidation capacity of the atmosphere.[7][8] Halogens have been shown to interact with reactive nitrogen species as well, such as NO_x (= NO + NO_2), N_2O_5, and NO_3, which not only influence reactive nitrogen concentrations locally, but can provide longer-range transport of NO_x i.e. via $ClNO_2$ and can contribute to ozone formation from certain reactive pathways.[9][10][11][12] Additionally, halogenated species have been demonstrated to affect the lifetime and cycling of volatile organic compounds (VOCs) and mercury (Hg) in the troposphere.[1][13][14][15][16]

The Marine Boundary Layer (MBL) is a critical sector of the global atmosphere for reactive halogen chemistry and its impacts on atmospheric composition. Previous studies have shown the importance of

examining and including MBL halogen chemistry in models to correctly predict O_3 and HO_x concentrations, in addition to the baseline photolysis and water vapor reactions.[17] The main sources of tropospheric gas-phase halogens are thought to originate from the oceans. The emission of sea salt aerosols (SSAs) is likely the dominant global source of reactive halogens, where chlorine and bromine are liberated from SSAs via acid displacement and debromination reactions (the largest source of inorganic iodine, however, is direct emission from the ocean). SSAs are produced in the marine environment by physical processes in ocean water such as wave breaking (generating sea spray), bubble bursting, and jet formation.[18] These aerosols have the most substantial impact on radiative forcing over the open ocean in the absence of cloud cover, in addition to being a source of cloud condensation nuclei (CCN) themselves.[19] Environmental factors such as relative humidity (RH) affect aerosol size, where higher humidity causes the swelling of particulates as they absorb water.[20] Emissions of photolabile organohalogens from biological activity in the ocean as well as reactive displacement from the ocean surface directly are also important, especially for bromine and iodine, respectively.[21][22][23][24] Herein, we focus on the sources, abundance, partitioning, and chemistry of reactive inorganic bromine, which has been shown to be particularly important in model simulations of the MBL ozone budget.[25]

Inorganic reactive bromine, Br_y (= Br + 2 Br_2 + HOBr + BrO + HBr + $BrONO_2$ + $BrNO_2$ + BrCl + IBr), is of particular importance due to its efficiency in ozone depletion events, and specific reactivity with other atmospheric components (such as mercury) with significant potential influence on air quality and climate. Relatively small concentrations of reactive bromine have been shown to have considerable impacts on tropospheric chemistry, interacting with NO_x, HO_x, O_3, and dimethyl-sulfide (DMS) cycles.[26] The largest global source of gaseous bromine species in the troposphere is thought to be the reactive debromination of sea-salt aerosols (SSAs).[27] Other sources of tropospheric Br_y include coal burning, volcanic eruptions, transport from the stratosphere, and photolysis of organohalogens emitted from the ocean.[28][29] The main sink mechanism for Br_y is uptake onto aerosol surfaces, with smaller contributions from wet and dry deposition.[25]

Simulations of reactive bromine chemistry typically find that bromine monoxide (BrO) and hypobromous acid (HOBr) are important components of Br_y reaction pathways, regulating the partitioning and recycling rates, and thus the efficiency of the associated catalytic ozone destruction cycle:

$$Br + O_3 \longrightarrow BrO + O_2 \tag{1}$$

$$BrO + BrO \longrightarrow 2\,Br + O_2 \tag{2}$$

$$BrO + HO_2 \longrightarrow HOBr + O_2 \quad (3)$$

$$HOBr + h\nu \longrightarrow OH + Br \quad (4)$$

The result of the above cycle is a net destruction of O_3 and the recycling of Br. Reactions 3 and 4 demonstrate the capability of Br_y to impact the ratio and concentration of HO_x, in this case via reacting with and reducing HO_2 in favor of producing OH. Reaction 3 is temperature-dependent (rate decreases with higher temperatures) and has been shown to also be influenced by the amount of water vapor present.[30][31] Because the gas-phase production of BrO and subsequently HOBr require free atomic bromine, they are expected to be highly dependent on active photochemistry and reach significant levels only in the presence of sufficient sunlight (e.g. daytime in the sub-tropical and tropical MBL). While this reaction chain is an important component in the destruction of ozone via bromine chemistry, it is not the only loss pathway of BrO, which is itself photolabile. It can also react with NO to reform free atomic bromine, or with NO_2 to form bromine nitrate ($BrONO_2$).

As BrO formation is the main loss of atomic bromine in the MBL (via reaction 1), its subsequent branching reactions and fate impacts the total concentration and distribution of Br_y among its constituent species. For example, HOBr and $BrONO_2$ are expected to have slightly different photolytic lifetimes, with that of HOBr around 12 minutes and that of $BrONO_2$ approximately 20 minutes during peak photolysis. Therefore the net rate of the above cycle will depend on the relative formation rates of HOBr and $BrONO_2$, i.e. on the BrO fate. There is also the possibility for BrO to react with chlorine monoxide (ClO) in the gas phase to form the interhalogen species, BrCl, in a reaction analogous to equation 2:

$$BrO + ClO \longrightarrow BrCl + O_2 \quad (5)$$

The first published observations of BrO were reported by Hausmann and Platt in 1994 using a Long-Path Direct Optical Absorption Spectroscopy (LP-DOAS) technique in the Arctic during springtime.[32] Mixing ratios up to 17 ppt (with a limit of detection of approximately 4 ppt) were reported. Multiple studies conducted in Arctic regions have produced observations of some tropospheric Br_y components, while coordinated measurements of Br_y outside of the Arctic remain sparse. Other studies have reported BrO concentrations in the MBL typically remaining below 10 ppt.[28][33] The majority of studies comparing modeled and observed reactive bromine mostly involve BrO, with few (if any) other components of Br_y. BrO concentrations remain near/below detection limits in many CIMS-based measurements, which causes uncertainty when comparing to model outputs and generates a need for more sensitive and comprehensive

Br_y measurements to assess chemical mechanisms.[25]

There are also multiple known heterogeneous reactions involving gas-phase reactive halogens on the surface of SSAs, which naturally contain aqueous phase halogen atoms present in seawater (Cl^-, Br^-, I^-). These reactions, depending on the species involved, produce dihalogen species which can then be liberated back to the gas phase, depleting the halide levels of salt particles. For reactive bromine, the main heterogeneous pathways involve the uptake of HOBr and/or $BrONO_2$ onto salt particles:

$$HOBr + X^-_{(aq)} + H^+_{(aq)} \longrightarrow BrX + H_2O \tag{6}$$

$$BrONO_2 + X^-_{(aq)} + H^+_{(aq)} \longrightarrow BrX + HNO_3 \tag{7}$$

$$BrONO_2 + H_2O \longrightarrow HOBr + HNO_3 \tag{8}$$

where X = Cl, Br, I.

Reactive bromine has been shown to react with organic aerosol (OA) as well, altering OA composition and potentially its ability to form CCN. Reduced BrO concentrations are observed by Buxmann et al (2015) when adding secondary organic aerosol (SOA) precursors to simulated SSA in chamber experiments compared to those with salt particles alone.[34] Halogenated compounds have even been reported to react with volatile organic compounds (VOCs) and form ultrafine particles themselves.[35]

1.2 Reactive Bromine in a Polluted MBL

As noted above, the presence of NO_2 can lead to the formation of $BrONO_2$ and thereby influence the partitioning and abundance of inorganic bromine via the following gas-phase reaction sequences:

$$BrO + NO_2 + M \rightleftharpoons BrONO_2 + M \tag{9}$$

$$BrONO_2 + h\nu \longrightarrow BrO + NO_2 \tag{10}$$

$$BrONO_2 + h\nu \longrightarrow Br + NO_3 \tag{11}$$

$$BrONO_2 + Br \longrightarrow Br_2 + NO_3 \tag{12}$$

Reactions 1 and 9 can affect the partitioning of NO and NO_2, and high NO_2 conditions can decrease HOBr formation. Reactions 1, 9, and 11 also represent a pathway where ozone can be potentially removed via $BrONO_2$ formation and subsequent reactions. Specifically, net destruction of O_3 occurs when $BrONO_2$ photolysis yields NO_3 and Br. However, under the active photochemistry required for this mechanism, NO_3

will also readily photolyze to produce NO_x, O_2, and O, complicating the efficiency of the destruction cycle given that NO_x in the troposphere will contribute to net ozone production.[36] There are also multi-phase pathways for both HOBr and $BrONO_2$ to react on or in aerosol particles, and thereby further influence reactive bromine concentrations at different rates (e.g. reactions 6-8).

The few studies of bromine chemistry in the polluted MBL have reported elevated BrO and/or Br_2 as measured by CIMS or DOAS, coincidental with relatively high NO_x levels, which typically stem from continental air masses influenced by anthropogenic activity and associated pollutants.[37][38] Enhanced Br_2 is also observed during the day in some cases, which typically implies a significant local source required to outpace the fast photolytic loss. In addition to possible point sources, such as power plants, explanations for this phenomenon have mostly included reactive nitrogen chemistry impacting halogen activation. Higher NO_x can lead to higher aerosol nitrate concentrations, which has the potential to increase the liberation of bromine from mixed aqueous particles containing both nitrate and bromide ions.[39] $BrONO_2$ can be taken up by SSA surfaces and react with aqueous HBr, HCl, and H_2O, to produce Br_2, BrCl, BrI, HOBr, etc., with a wide range of uptake rates reported depending on environmental factors such as pH. Calculated multi-phase reaction rates of HOBr with dissolved halogens in SSAs, for example, are updated based on laboratory experiments and parameterized in GEOS-Chem to increase as pH decreases (between values of 2 and 9, with constant rates outside this range), along with typical sea salt halogen concentration and thermodynamic considerations. Bromine nitrate hydrolysis also contributes to a global sink of NO_x in the model.[25] $BrONO_2$ is thought to play a large role in halogen release from SSA under high NO_x conditions through such heterogeneous chemistry. In such environments the BrO + NO_2 reaction would be highly favored and Br_y compounds would likely be converted back to $BrONO_2$ during the day.[40] There is also an established mechanism for the uptake of N_2O_5 on halide-rich SSA to form $ClNO_2$, $BrNO_2$ and INO_2, which would potentially also be active during high NO_x conditions.[41]

Several questions and uncertainties remain regarding the effect of pollution and elevated NO_x on bromine chemistry in the MBL, as well as the multi-phase cycling of reactive halogens. These include how the presence of NO_x affects the partitioning of Br_y, particularly between HOBr and $BrONO_2$ and the subsequent recycling of dihalogens from multi-phase chemistry with SSAs. Here, we present results containing simultaneous observations of five components of atmospheric Br_y in the semi-remote subtropical MBL of Bermuda. This work includes direct simultaneous observations of both HOBr and (for the first time, to our knowledge) $BrONO_2$. We illustrate with these observations that current parameterizations of reactive bromine chemistry are likely in error by several factors in terms of the abundance and partitioning of Br_y for this region.

2 Methods

2.1 Field Campaign Description and Instrument Setup

The Bermuda boundary Layer Experiment on the Atmospheric Chemistry of Halogens (BLEACH) field campaign took place over two six-week legs, in May-June 2022 as well as January-February 2023. The purpose of the campaign is to investigate halogen chemistry in the MBL through a suite of gas and particle-phase measurements of chlorine, bromine, and iodine-containing species in the ambient atmosphere. BLEACH also represents the first field deployment of the atmospheric pressure transverse ion-molecule reaction region or t-IMR-equipped HR-ToF-CIMS.[42] The measurements took place at the Tudor Hill Marine Atmospheric Observatory (THMAO) located on the southwestern shores of Bermuda, operated by the Bermuda Institute of Ocean Sciences (BIOS). The site is situated approximately 40 meters from the coastline, ∼30 m above the sea surface, and is relatively secluded from main roads and other structures in the immediate surrounding area. The site location and prevailing winds enable observations of marine boundary air that has spent several hours to days over the open Atlantic Ocean, with intermittent periods of influence from both relatively smaller-scale local anthropogenic activity as well as long-range transport of polluted air from the east coast of the United States. There have been multiple atmospheric studies conducted at THMAO to investigate NO_x, HO_x, and O_3 chemistry, with few direct observations of halogen-containing compounds.[43][44][45][46]

The iodide-mode t-IMR-ToF-CIMS (henceforth abbreviated as the t-CIMS) was stationed atop a 10 meter tall tower temporarily erected at the site, complemented by a suite of other instruments including (on the same tower) another HR-ToF-CIMS operated with a low-pressure VOCUS-AIM IMR, capable of operating in both iodide and bromine-adduct ionization modes, a Tunable Infrared Laser Direct Absorption Spectrometer (TILDAS) measuring hydrochloric acid (HCl), and a spectral radiometer. Also present on the ground at the site was an LP-DOAS instrument positioned with a measurement path over the ocean to a reflector approximately 10 km from the light source and detector. Atop the permanent THMAO 23-meter sampling tower was a Laser-Induced Fluorescence (LIF) instrument measuring NO_x[47], a chemiluminescence instrument measuring ozone, a cascade impactor collecting and separating aerosols by aerodynamic size onto filters to be analyzed offline, and a suite of meteorological instruments providing measurements of humidity, wind speed/direction, temperature, and precipitation.

The t-CIMS was operated from inside weather-proof housing with ports only for power lines, the IMR inlet, and a small air conditioning unit used to assist in stabilizing instrument temperature. Ambient air was drawn at 110 L/min through a 15" long, 3" outer diameter (OD) Aluminum tube using an Agilent model SH110 pump connected through two symmetrically positioned ports located downstream where the duct mounted to the weatherproof instrument enclosure. This outer duct is comprised of brushed aluminum, and

the underside of the inlet face was cut at a 45-degree angle such that the longer side acted as a rain shield for the t-IMR inlet. The large flow through the duct serves to move air to the t-IMR inlet while also damping turbulent eddies prior to sampling the air into a 1" OD Teflon tube that ran axially down most of the inner length of the outer 3" OD duct, and served as the t-IMR inlet. A flow of 10 L/min was sub-sampled by the atmospheric pressure t-IMR through the 1" OD Teflon tube. The residence time of air in the outer duct is calculated to be 0.75 seconds, and the residence time in the t-IMR is another 0.76 s.

The t-IMR is operated at a 1 Hz sampling frequency, producing a mass spectrum every 1 second. Iodide reagent ions are produced via a 1.5 L/min flow of UHP N_2 gas over a CH_3I permeation device located inside the climate-controlled t-CIMS enclosure, mixed with a much smaller 2 sccm flow over the head space of a liquid toluene vial (containing between 3-5 mL toluene, $C_6H_5CH_3$) and ionized with a vacuum ultraviolet (VUV) lamp contained in stainless steel housing with a 1.5 kV potential applied at the exit into the t-IMR cavity, also described previously.[42] The IMR flow is measured at startup using an analog ball meter fixed to the 1" OD inlet (prior to the secondary inlet installation) while the IDP3 pump is throttled using a needle valve until the desired 10 L/min flow is achieved. The 3" secondary inlet is secured concentrically around the IMR entrance with aluminum blocks to stabilize the inlet, along with rubber O-rings sealing all stages of the inlet apparatus to the weather-proof housing box and around pumping ports.

Instrument background signals are determined by overflowing the t-IMR chamber with UHP nitrogen at flows typically between 12-14 LPM (at minimum greater than 10 LPM) for a time period of at least 2 minutes. This was achieved during the campaign by manually maneuvering a 1/2" OD tube (PTFE with stainless fittings) through the outer duct and directly in front of the IMR entrance while controlling N_2 output flow with an Alicat mass flow controller (MFC). The signals for a given peak in the mass spectrum during such "zero" or instrument background periods used in calculating the limit of detection (LOD) for that specific compound, per the equation published by Bertram et al 2011[48]:

$$\frac{S}{N} = \frac{C_f[X]t}{\sqrt{C_f[X]t + 2S_0t}} \tag{13}$$

Where S/N is the signal-to-noise ratio, C_f is the calibration factor for molecule X, $[X]$ is its concentration, S_0 is the signal during a zero or background determination for molecule X, and t is the integration time for its given peak in the mass spectrum. A standard S/N ratio of 3 is applied, which is used in conjunction with measured background signals, defined sensitivities and integration times to calculate the minimum measurable concentration or instrument LOD, $[X]$. Background signals are extrapolated and subtracted from those during observations before converting to units of concentration.

2.2 Direct Instrument Calibration

Throughout the campaign, the t-CIMS was calibrated multiple times for Br_2 by adding a known concentration to the IMR for a short period and monitoring the resulting integrated peak signal at the isotopically constrained $Br_2(I^-)$ mass-to-charge (m/Q) ratio. Bromine gas is produced via a commercially purchased KIN-TEK™permeation tube with a published output rate of 140 ng/min at 40°C, which was verified gravimetrically to be within the manufacturer reported error (± 5 ng/min) of the device. The permeation tube is kept in a custom-built incubator which utilizes PTFE housing and fittings, heating tape and thermocouple to keep the temperature of the device constant at 40°C. The gaseous Br_2 is delivered via a carrier flow of 40 standard cubic centimeters per minute (sccm) of ultra-high purity (UHP) nitrogen gas directly to the t-IMR (bypassing the secondary inlet) or to an exhaust line when not in use. With these parameters, the concentration of any gas, X (C_X), in pptv in the IMR at the time of calibration can be calculated assuming stable conditions:

$$C_X = \frac{\delta_X}{m_{mol}} \frac{1}{F} K_g T \cdot 10^{12} \tag{14}$$

where δ_X is the permeation rate of gas X in ng/min, m_{mol} is the molar mass of gas X in ng/mol, F is the largest flow in which the permeation device output is diluted (the t-IMR flow in this case) in sccm, T is temperature in Kelvin, and K_g is the universal gas constant: 82.06 $\frac{cm^3 atm}{K\ mol}$. With C_x and the measured signal of gas X normalized to Total Reagent Ion Counts (TRIC = I^- + IH_2O^- signals), a sensitivity value or calibration factor can be calculated and reported in units of counts ppt^{-1}. A group of four robust calibrations of Br_2 performed during the winter leg of the campaign (BLEACH23) are used at the native resolution of 1 Hz to determine instrument sensitivity. Calibration periods i.e. the manual addition of gaseous bromine flow are determined from clear and stable increases in the Br_2I^- cluster signal. All viable data points across the four calibrations yield a mean sensitivity of 1.5 (± 0.4) counts ppt^{-1}. Given the negligible carrier flow of bromine gas compared to that of the t-IMR flow (ratio of 0.4%), the IMR humidity during the calibrations is assumed equivalent to ambient conditions, which for all calibration periods ranged from RH 68-77%. An experimental direct calibration method for HOBr is also performed, resulting in a range of the sensitivity ratio $\frac{C_{HOBr}}{C_{Br_2}}$ of 0.55 to 1. See supplemental section S.3 for further detail.

2.3 Iodide-Adduct Binding Enthalpies for Sensitivity Estimation

Given that multiple halogen-containing species detected with the t-CIMS during BLEACH are not commercially available or easily synthesized for reliable direct calibration, other methods to determine their sensitivities are of critical interest. Work conducted by Iyer et al (2016) demonstrates a strong correlation between the CIMS instrument sensitivity and corresponding binding enthalpy for a given molecule to the

Compound	Binding Enthalpy (kcal/mol)	Sensitivity (counts ppt^{-}1)
Br_2	24.3	1.51
HOBr	15.1	1.29
BrO	13.5	1.26
$BrONO_2$	13.3	1.25
BrCl	24.2	1.51

Table 1: Relative binding enthalpies and corresponding sensitivity (per 1e6 TRIC) for five key bromine gas phase species detected by the t-CIMS during BLEACH. The median TRIC for the campaign is 5.5e6.

iodide reagent ion.[49] In this study, a linear correlation is found between the logarithm of the directly measured sensitivity and binding enthalpy, $\log C_f \propto \Delta H$. For specific application to our halogen observations during BLEACH, the binding enthalpies for several key bromine and chlorine-containing molecules are calculated. Using the calculated binding enthalpies, a sensitivity value via direct calibration for Br_2, and the log-linear relationship, the instrument sensitivity for the other halogenated species is determined using the following relationship:

$$\frac{\log C_{f,X}}{\log C_{f,Br2}} = \frac{\Delta H_X}{\Delta H_{Br2}} \Rightarrow C_{f,X} = C_{f,Br2}^{\left(\frac{\Delta H_X}{\Delta H_{Br2}}\right)} \tag{15}$$

Here $C_{f,X}$ is the CIMS sensitivity determined for molecule X and ΔH_X is its given binding enthalpy to I^-. Geometries of the free molecules and the molecular clusters are optimized at the PBEPBE/aug-cc-pVTZ-PP level of theory using the Gaussian 16 program.[50][51][52] Iodine and bromine pseudopotential definitions are taken from the Environmental Molecular Sciences Laboratory (EMSL) basis set library. The final energies are refined at the DLPNO-CCSD(T)/def2-QZVPP level of theory using the ORCA program version 4.2.1.[53][54][55][56][57][58] Shown in Table 1 are the key bromine-containing species with their corresponding calculated binding enthalpies and subsequent instrument sensitivity for the in-situ calibrations during BLEACH, determined via equation 15. The fractional sensitivity of HOBr to Br_2 using this binding enthalpy method is calculated to be ~ 0.8, which is within the experimental range determined in section S.3 and is also in reasonable agreement to the study by Liao et al (2011) referenced therein. The sensitivity ratio of BrO to Br_2 is also approximately 0.8, which is consistent with another study by Liao and coauthors (2012).[59] Our experimental calibration to directly determine an instrument sensitivity range for HOBr along with the values previously reported all serve as independent validation for this binding enthalpy method for reporting concentrations of the detected Br_y.

2.4 Water Vapor-Dependent Sensitivity Values

Iodide-adduct CIMS sensitivity for many compounds is dependent on the humidity, or more specifically, the partial pressure of water vapor (P_{H2O}) present in the IMR, which is also related to temperature and pressure

in the IMR.[60][61][62][63] A dynamic P_{H2O}-based sensitivity correction for Br_2 developed previously using laboratory experiments and the direct in-field Br_2 calibrations is used to generate sensitivity timeseries for all measured Br_y components during BLEACH23.[42] Integrated signal counts for these compounds (clustered to the iodide reagent) are normalized to TRIC and subsequently divided by this dynamic sensitivity, point-by-point, to produce concentration values reported in parts per trillion (ppt) by volume at each 1-minute time step.

2.5 Uncertainty Considerations

Multiple uncertainties exist in the measurement and conversion of Br_y component signals to ambient concentration (ppt), for which we employ either published/empirical values or upper limit estimates. These include uncertainties in the Br_2 permeation tube output, mentioned previously to be ± 5 ng/min, the laminar flow rate through the IMR estimated as an upper limit to be ± 2 LPM, binding enthalpies assumed to be within ± 1.6 kcal/mol[64], and a standard deviation of detected signals averaged over 1-minute calculated to be ± 20%. We propagate these values through our calculations and present them as $\pm 1\sigma$ for median diel concentrations in figure 3.

In addition to these random sources of error, systematic biases arise from wall interactions and possible loss or chemical conversion of ambient analytes. While the t-IMR has significantly reduced wall effects compared to typical low-pressure Iodide ionization regions, the possibility of conversion on inlet surfaces, particularly via heterogeneous Br_y chemistry on water droplets and salt particles deposited onto the t-IMR inner cavity, remains a possibility. Calibration standards for the Br_y compounds most likely to react with salt and water droplets are not readily available (e.g. HOBr and $BrONO_2$) in pure forms. Therefore, to estimate this effect, we calculate the fraction of sampled air mass that theoretically has *not* interacted with the walls of the IMR cavity by the time it reached the sampling port of the MS (f_0), according to the equation:

$$f_0 = exp(-3.66 \cdot \frac{D_g}{P \cdot r_{IMR}^2} t_{res}) \tag{16}$$

where D_g is the gas phase diffusivity, P is the pressure in the IMR (1 atm), r_{IMR} is the inner radius of the IMR cavity (1.11 cm), and t_{res} is the residence time of the t-IMR. We use the largest calculated (using temperature and pressure observations) D_g value of 0.14 $cm^2 s^{-1}$ for the Br_y compounds detected during BLEACH. This equation assumes laminar flow and is used at standard temperature and pressure (298 K and 1 atm) to produce an f_0 value of 0.75, which means that an upper limit of 25% of sampled air interacts with the walls of the t-IMR cavity. We further assume for these purposes that any wall interaction results in a loss or conversion into another detected species.

2.6 Particle Measurements

The cascade impactor used for aerosol speciation is positioned on the permanent 23 m tower at THMAO, utilizing a high volume air sampler for particle collection. The high volume flows of ∼800 L/min are turned off during any period of work requiring personnel on the tower to prevent contamination. The quartz filters used (TE-QMA and TE-230-QZ) are rinsed in 18 MΩ cm water and combusted at 500°C before use. The data presented in this work for BLEACH23 includes 5 aerosol size-cutoff bins based on aerodynamic diameter at the 50% collection efficiency (D_p50), in addition to the bulk concentrations (all sizes). The bin sizes are < 0.6 μm, $0.6 - 0.9$ μm, $0.9 - 2.3$ μm, $2.3 - 11$ μm, and > 11 μm. Active collection for a filter occurred typically at a frequency of ∼24 hours, with sampling starting around 09:30 local time and stopping the following morning at 09:00 when the filters would be changed. Some extreme weather events prevented filter exchange, resulting in longer sampling periods.

The filters were analyzed offline in the University of Washington laboratory, where they were cut into small pieces and placed in a 50 mL centrifuge tube containing 20 mL of 18 MΩ-cm water. The tube was then weighed and shaken for 30 minutes. Insoluble material is removed from the tube using a 0.2 μm poly(ether sulfone) syringe filter. The centrifuge tube and filter masses (after liquid removal) were used to calculate the yield during sample extraction. Field blanks were acquired by loading a set of filters in the cascade impactor and placing it into the container used to climb the tower. Four sets of field blanks were collected in the summer and 9 sets in the winter (yielding 8 and 63 total blank filters, respectively). Samples were blank-corrected according to size bin. Yields during this extraction and the calculated total volume during in-situ sampling were used to report ambient aerosol species concentrations in μg m^{-3} .

A coupled ion chromatography (IC) technique was used to measure all species except iodine. A Dionex AS-DV autosampler divided a 2.5 mL sample between a Dionex ICS-2000 for anions and a Dionex Integrion HPIC for cations. The autosampler operated in loop mode with a delivery speed of 4.0 mL/min, a delay volume of 1.25 μL to coincide with the sample loop, a 250 μL rinse with 18 MΩ-cm water, and a flush factor of 10. The Dionex ICS-2000 was equipped with a Dionex IonPac AS20 RFIC 2 x 250 mm analytical column. The instrument method utilized a 60-minute multi-step eluent gradient of KOH (5/30/55 mM) to achieve complete separation of species. Cation species were measured using the Dionex Integrion High-Performance IC, equipped with a Dionex IonPac CS12A RFIC 4 x 250 mm analytical column, and a multi-step eluent gradient of MSA (3.25/19.5/30 mM). Species measured using this technique include sodium (Na^+), calcium (Ca^+), magnesium (Mg^+), chloride (Cl^-), bromide (Br^-), nitrate (NO_3^-), and sulfate (SO_4^{2-}).

Total aerosol iodine (a mixture of iodide, iodate, and soluble organic iodine) was measured using Inductively Coupled Plasma Mass Spectrometry (ICP-MS) at Trace Lab (University of Washington School of

Oceanography) using an iCap RQ ICP-MS and a modified EPA 6020B analytical protocol. Samples were aspirated in a capillary tube using a PFA nebulizer and aerosolized in a quartz cyclonic spray chamber before injection into the plasma. A collision-reaction cell (CRC) within the iCap RQ was used with helium as a collision gas in kinetic energy discrimination (KED) mode to reduce isobaric interferences and improve signal stability. Because certain iodine species (e.g., I^-) have lower mobility, a longer washout time was used (2-3 minutes) after each sample analysis. ^{123}Rhodium was used to monitor signal drift throughout sample analysis, while memory effects were monitored via the blank injections of 18 MΩ-cm water in between sets of samples. Ambient aerosol observations and their propagated errors are publicly available in the University of Washington data repository with summary statistics in Table S1 (see data availability section). Detailed ICP-MS parameters are listed in Table S2.

2.7 GEOS-Chem Model Description

The GEOS-Chem high-performance model version 14.2.3 is used to simulate and examine halogen chemistry in the MBL to compare with observations at THMAO. Stretched grid simulations are used to increase the spatial resolution of the grid box containing the field site to 70 square kilometers. The specific resolution used is C48 S3 with the location of Bermuda at 32.25°N 64.75°W as the center target. The model utilizes MERRA-2 meteorological fields from the NASA Global Modeling and Assimilation Office. A 22 month spin-up period is implemented from July 2020 to May 2022 for species to reach equilibrium and provide initial conditions more relevant to actual conditions. Tropospheric halogen chemistry in the model is handled according to the systems of reactions described most recently in Wang et al 2021, building upon results reported by Sherwen et al 2016 and Chen et al 2017.[25][65][66] The sea-salt debromination mechanism is included in the model run as is the default for this version. Sea-salt aerosol emissions are the largest source of tropospheric inorganic halogens in the model, with a small contribution from organohalogen emissions and stratospheric exchange. For iodine species, direct emission from oceans in the form of I_2 and HOI is considered as the largest source. Wet and dry deposition contribute (approximately equally for each for all three halogens) as the largest sink for chlorine and iodine species. Wet and dry deposition is a relatively much smaller sink than aerosol uptake for modeled bromine. Hourly output is extracted for both summer and winter legs of the BLEACH campaign. Here, we focus on comparison with the wintertime run spanning from January 15 to February 12 2023.

3 Reactive Bromine Observations

Shown in figure 1 are the 15-minute average (water-vapor-corrected) concentration timeseries of five reactive bromine species measured with the t-CIMS at THMAO, adjusted to local time of sampling (Bermuda, UTC - 4). See supplemental section S.1 for more details on the high resolution spectral identification of observed reactive bromine species. The missing portion of data from Feb 2-8 2023 is due to a nationwide power-outage in Bermuda and subsequent efforts to bring site instruments back online. Concentrations for all measured Br_y species other than HOBr show a shift to lower concentrations around Jan 27 and 28 and remain relatively small for the rest of the sampling period. All components show the highest average levels before these dates with episodic trends depending on time of day for some, and larger time scale variation for others.

Figure 2 shows wind roses for the Br_{y*}^{g} ($= 2\,Br_2 + HOBr + BrONO_2 + BrO + BrCl$) compounds measured during the winter deployment. The t-CIMS data is coordinated with 1-minute wind speed and direction data from the 23m tower at THMAO, and then binned into the displayed sectors for wind direction. To ensure that the wind direction bins are robust, data coinciding with wind speeds below 0.2 m/s are excluded (less than 2% of all t-CIMS data coverage). Each wind rose only includes data for which concentrations of the given compound are above the respective (1 minute) detection limit, so the wind direction frequencies (wedge radii) deviate slightly between compounds due to different measurement periods being excluded. Also shown in the bottom right panel of figure 2 is a satellite image of the THMAO site with a purple marker showing the location of the t-CIMS measurements onsite and within the island. The inset in the image is a uniformly colored wind rose to show the frequency of all wind direction measurements during the BLEACH23 t-CIMS sampling period. The standard criteria used at THMAO for determining onshore winds is to include only wind direction measurements between 210°and 315°(where 0°is true North), representing the southwesterly to northwesterly sector in the wind rose. This sector is indicated with green dashed lines in the inset, which we take as conservative bounds on marine-influenced air masses.

BrO measurements have a relatively low average concentration of 0.06 ppt (below the 1-minute LOD of 0.11 ppt) and a maximum of 0.28 ppt. Consistently low concentrations measured for BrO are somewhat expected in the subtropical MBL given its relatively high reactivity, including the second largest photolysis rate behind Br_2 among all bromine species presented. However, because BrO detection during BLEACH23 is so sparse, with only ∼6% of all 1-minute measurements above LOD, we do not have confidence to interpret it beyond an "upper limit" and therefore exclude its diel trend and further independent analysis. We also note that LP-DOAS measurements of BrO remained below detection limits throughout the measurement period.

The diurnal cycles for detected Br_y species (except BrO) are given in figure 3. In order to reduce

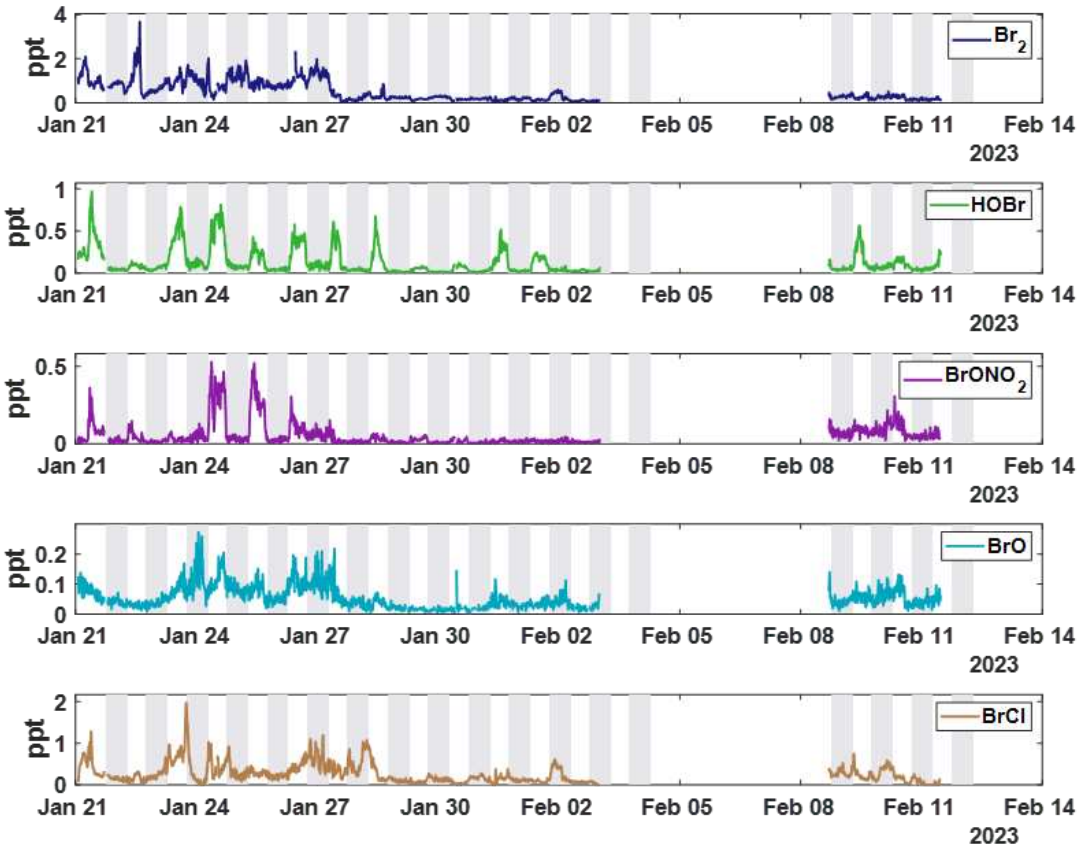

Figure 1: 15 minute averaged concentration timeseries of Br_2, HOBr, $BrONO_2$, BrO, and BrCl as measured by the t-CIMS at THMAO during the wintertime BLEACH23 campaign. Background shading in gray represents hours between sunset and sunrise (18:00-06:59 local time).

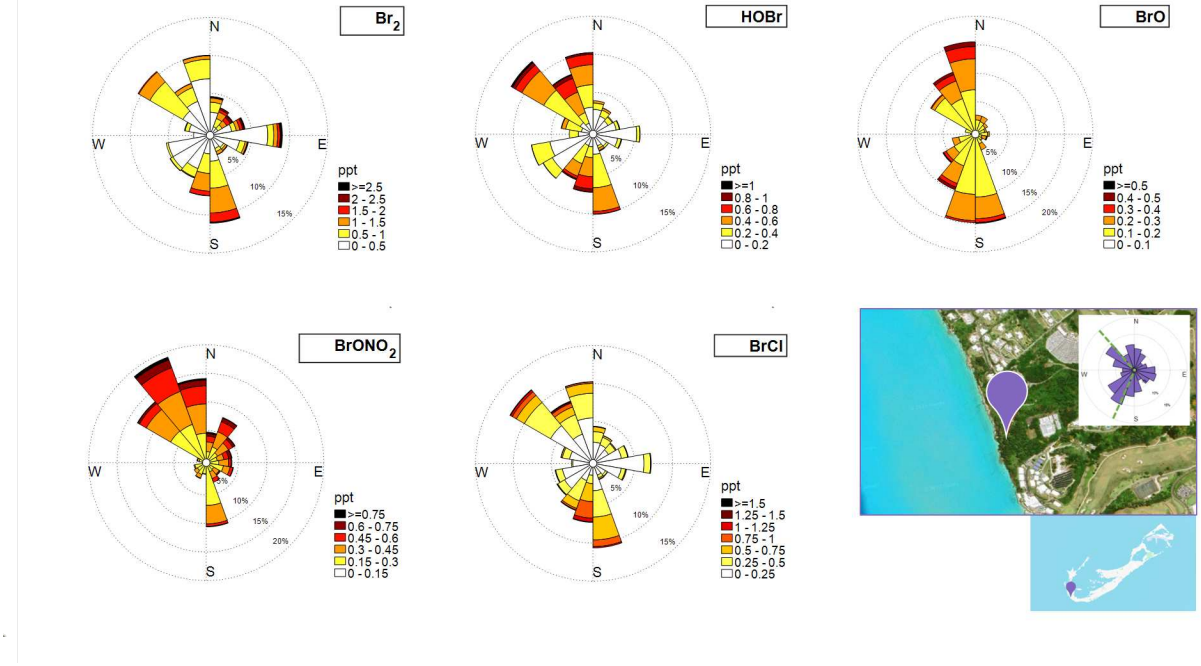

Figure 2: Wind roses of five Br_y species measured during BLEACH23. Wedge radii represent the percentage of 1-minute data points that fall into the corresponding wind direction sector. The radial length of each wedge represents the corresponding fraction of sample points that fall into that sector. Wedges are colored by corresponding species concentration frequency as noted in the legend of each plot. The scaling of this color map changes with each compound. Points with wind speeds below 0.2 m/s and concentrations below LOD for each compound are not included in the respective plot. A satellite image of the THMAO site (purple marker) is also included in the bottom right with a map of Bermuda [Google maps], as well as a wind rose of the frequency of wind directions for the entire t-CIMS sampling period.

interference from local anthropogenic activity on the island, these diel trends reflect measurements taken during periods of onshore winds, including only data points where the rolling 30-minute median observed wind direction is between 210-315°and wind speeds are above 0.2 m/s. Diel trends using all campaign data can be found in supplemental figure S4. For reference, the local sunrise and sunset times on Jan 20 are respectively 07:19 and 17:41; and for the final day of sampling on Feb 11 they are 07:06 and 18:02.

Br_2 generally shows the highest concentrations relative to the other key Br^g_{y*} species, with a maximum concentration of 3.7 ppt in the 15-minute average. The median concentration in the diurnal cycle stays below 1 ppt, with a mean concentration of 0.4 ppt for all onshore wind data. There is a clear decrease in concentration after the morning of January 27, which marks a distinct shift in the levels of multiple components of Br^g_{y*}. Due to relatively large photolysis rates (photolytic lifetime on the order of 45-60 s at midday), Br_2 is expected to decrease to near if not completely below detection limits during the day, according to multiple model outputs and previous work. While concentrations are higher during the nighttime hours, there is a lack of a decrease and even small enhancement around midday, which becomes more apparent when looking at the 75^{th} percentile of the measurements. A significant daytime source of Br_2 would be required to compensate for and overtake the large photolytic sink for daytime periods in which concentrations remain above LOD. Nearly all data points in the 1-minute timeseries are above LOD for Br_2. As mentioned previously, there is potentially systematic error in that up to 25% of sampled air masses may come into contact with instrument surfaces, which could convert ambient HOBr and $BrONO_2$ to Br_2, creating artificial signal. However, even if the conversion rate is assumed to be unity, i.e. that contact with surfaces always results in conversion of these two species to Br_2, daytime levels remain between 0.1-0.2 ppt (when subtracting 25% of observed HOBr+$BrONO_2$ signals), well above detection limits, and still a local enhancement around midday in the 75^{th} percentile. The wind rose for Br_2 shows the most uniform spread in direction, with slightly more data in the westerly wind sector. It also shows the lowest dependence of concentration on wind direction among Br^g_{y*} species, with elevated levels shown in almost every wedge. There are infrequent yet strong enhancements in the north to easterly directions, showing the highest concentrations indicated in the dark red and black colors.

We report an average concentration of 0.13 ppt for HOBr and maximum of 1 ppt in the 15-minute binned average for all of BLEACH23. Signals reliably increase each day after sunrise, mostly peaking in late morning and returning to near/below detection limits during the nighttime. This behavior is consistent with the current understanding that HOBr production in the gas phase depends on the presence of BrO, which is produced via photolysis-driven reactions that result in free atomic bromine in the atmosphere. Compared to the other Br^g_{y*} species, there is less of a noticeable drop in HOBr signal after Jan 27^{th}, recording similar daytime maximum concentrations.

While hourly median concentrations of $BrONO_2$ remain close to LOD, there is a clear a daytime enhancement in signal, particularly in the 75^{th} percentile shading, and very low/below LOD concentrations at night. The average and maximum concentrations for the campaign respectively are 0.04 and 0.35 ppt. Similarly to HOBr, the diel behavior of $BrONO_2$ aligns with known chemistry requiring photolytically-dependent BrO as a necessary precursor for its gas-phase production. Liao et al (2012) in their study present a model-predicted $BrONO_2$ diel trend, showing increased concentrations during the day and a local minimum around midday, attributed to a rapid increase in the bromine nitrate photolysis rate.[2] It is also possible that under a NO_2-limited regime, higher NO_2 photolysis during midday i.e. NO_x equilibrium shifting toward NO, would reduce available NO_2 for reaction with BrO to form $BrONO_2$. The onshore wind criteria limits the inclusion of the few days with prominent bromine nitrate signal from the t-CIMS (see fig 1). The profile in figure S4 including all BLEACH23 data exhibits a very similar shape to that of Liao and coauthors, with two local maxima in the early morning at 8 am (0.05 ppt) and in the afternoon at 3 pm (0.03 ppt), revealing a small local minimum between where the strongest photolysis rates are expected on days with minimal cloud cover. Given that the photolysis loss rate of $BrONO_2$ is calculated to be less than that of HOBr, which shows no local minimum during midday in the campaign-long diel trend, we postulate that THMAO may indeed be in an NO_2-dependent regime concerning bromine nitrate production.

Similarly to Br_2, $BrONO_2$ also shows elevated concentrations detected with winds out of the northeastern sector, though the highest frequency and elevated concentrations for bromine nitrate are shown in the northwesterly wind sector. The north through southeasterly wind sector ($\sim$0 - 120°) includes air masses most directly affected by local anthropogenic pollution and land influence. This sector also shows much higher NO_x both in frequency and in concentration compared to the westerly directions, typically on the order of several hundred ppt up to a few ppb. This is unsurprising as the easterly direction encompasses nearly all local anthropogenic activity, including the island's only city of Hamilton and power plant located approximately 9 km from THMAO with a heading between 60-75°. Figure S5 displays a wind rose for NO_x concentrations at THMAO, highlighting the large directional gradient and influence of local pollution on reactive bromine chemistry, showing higher concentrations in many of the same wedges as $BrONO_2$ and Br_2.

Concentrations for the interhalogen species BrCl show an average of 0.26 ppt and a maximum at 2.6 ppt. There are multiple heterogeneous reaction pathways for which BrCl can be produced via HOBr, HOCl, $BrONO_2$, and $ClONO_2$ reacting with aqueous chloride and bromide in and on the surfaces or SSA particles. There is also the gas phase formation pathway involving BrO reacting with ClO (reaction 5), which the iodide adduct t-CIMS was not able to detect during BLEACH23. BrCl concentrations exhibit a similar drop in concentrations to the rest of Br^g_{y*} for the second half of the campaign, though in this case falling slightly later, after Jan 28. The diurnal profile of BrCl shows decrease in concentration starting around sunrise, though

still remains significantly above LOD with a relative increase in the late morning-early afternoon hours. Similar to Br_2, the persistence of BrCl concentrations (even when accounting for potential inlet conversion) throughout daylight hours in the diel trend is somewhat surprising given that it also has a relatively large photolysis loss rate.

The HOBr and BrCl wind roses show a clear enhancement in concentrations as well as frequency of measurement above LOD mostly in the western half of their respective wind roses, with much lower concentrations coming from the east. The coincidence of higher HOBr and BrCl concentrations in figure 2 with local winds coming from the northwest, southwest, and (as a more marginal case) southern directions implies a marine/coastal origin or at least influence in their atmospheric chemical sources. This likely stems from gas phase transformations of free atomic bromine (Br) during the day, the source of which can be attributed to photolysis of most Br_y species present in the MBL. This includes compounds liberated from and formed on the surfaces of SSAs. Reaction pathways for the formation and emission from aerosol surfaces for Br_2, BrCl, and HOBr have been reported.[65] Br is expected to rapidly form BrO, which as stated previously is considered highly reactive as well as photolabile, acting as a branching point for the inorganic bromine chemical mechanism in the presence of sunlight. The enhancements of Br_2 and $BrONO_2$ with northwesterly winds imply a similar marine-influenced source discussed for the other Br^g_{y*} compounds in that wind sector. However, the coincidence of some of the highest Br_2 and $BrONO_2$ concentrations with winds from the north*easterly* sector suggest an additional local island-based source of bromine, and/or pollution-driven increases in production. Formation of $BrONO_2$ is considered exclusive to reaction 9, dependent on the presence of NO_2 and BrO as reactants. This behavior is consistent with the generally much higher levels of NO_x measured for local easterly winds (see figure S5). $BrONO_2$ also has the longest photolytic lifetime among the Br^g_{y*} components, potentially contributing to why it may remain elevated in the eastern wind sector while HOBr and BrO do not. On the other hand, Br_2 also has its highest concentrations registered in the easterly sector and has the highest photolysis loss rate. Thus, a single common source and differences in photolytic loss rates alone are not enough to explain this enhancement for both compounds. It seems probable that there exists some or multiple local bromine-containing emission source(s) to the east of THMAO and, in the presence of elevated NO_x from anthropogenic activity (local or otherwise), $BrONO_2$ is quickly and preferentially formed over HOBr. The source(s) could be a strong emitter of diatomic bromine, or secondary reactions (i.e. on SSA surfaces) quickly recycling Br_2 from $BrONO_2$ (and HOBr) to the gas phase to compensate it's relatively much shorter photolysis lifetime.

The possibilities considered for such a local source of reactive bromine include the power plant located in Hamilton, anthropogenic activity (e.g. small scale coal burning, pool and jacuzzi maintenance, etc.) and enhanced direct organobromide emissions from macroalgae in the Great Bay or other coastlines to the east of

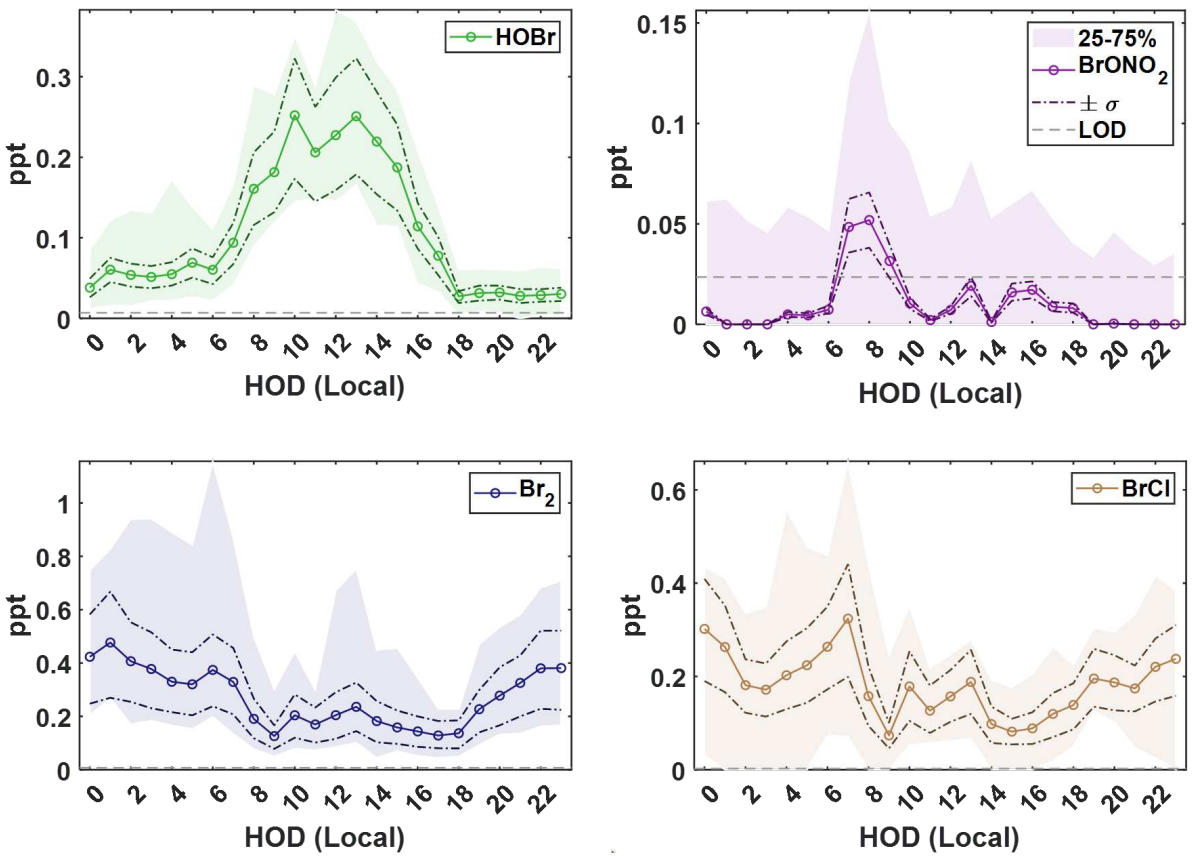

Figure 3: Diurnal profiles o HOBr, $BrONO_2$, Br_2, and BrCl as measured by the t-CIMS at THMAO during the BLEACH23 campaign, including only periods with onshore winds. Open circle traces show the median concentration for the given compound at each hour of the day for all included points, shading represents the 25^{th} to 75^{th} percentile concentrations, and the darker color dot-dashed traces show the median $\pm 1\sigma$ of propagated uncertainty in concentration. Gray dashed lines indicate the LOD calculated for each compound via equation 14 (for 1-hour time resolution).

THMAO. While bromine has been detected at relatively large levels in coal-burning power plant plumes[11], to the best of our knowledge the plant operating in Hamilton uses heavy fuel oil and diesel as fuel.[67] Wind speeds for the NE/E wind sector throughout the campaign were relatively calmer, with a median of 1.7 and maximum of 6.5 m/s for directions between 0-120°, compared to a respective median and maximum of 4.9 and 18.1 m/s for all directions. This along with the distance of ∼9 km between the plant and the nearly ground-level t-CIMS sampling location makes power plant exhaust unlikely to be the cause of the easterly enhancement. Average NO_x concentrations in this easterly sector register a mean value of 980 ppt, compared to the mean of 80 ppt for the conservatively defined onshore wind sector (210-315°). As mentioned in the introduction, polluted environments and elevated NO_x have previously coincided with increases in observed Br_y, associated with either unknown local sources and/or changes in heterogeneous chemistry via higher aerosol nitrate and changes to pH.

Given that $BrONO_2$ and HOBr both depend on the photolytic production of BrO during the day, examining the relationship or lack thereof between the concentrations of the two is important for evaluating existing chemical mechanisms and identifying favorable conditions for one product pathway vs. the other. Shown in figure 4 is a scatter plot of 15-minute-averaged $BrONO_2$ vs. HOBr concentrations for the entire BLEACH23 campaign as measured by the t-CIMS (including the easterly wind sector), colored by bins of NO_2 concentrations reported in ppt as measured by the onsite LIF instrument. The 1:1 line is shown in the light gray dashed trace for reference of a linear relationship case. Generally speaking, both compounds are shown to have coincident enhancements. However, a linear regression fit results in a slope (m) of 0.26 and a correlation coefficient (R value) of 0.53. There is a clear trend showing that as NO_2 levels increase, the two become more tightly correlated and $BrONO_2$ production is more favored as evidenced by the increasing slope toward the 1:1 line.

As the NO_2 bins increase in concentration, the slope of the linear fit increases, as does the correlation coefficient, with m = 0.02 and R = 0.08 for NO_2 < 100 ppt, m = 0.31 and R = 0.74 for 100-250 ppt, and finally maximizing with m = 0.93 and R = 0.77 when NO_2 is above 250 ppt. This indicates more clearly that $BrONO_2$ production becomes much more favorable than (yet still trends with) the production of HOBr at the higher NO_2 levels, corroborated by the maximum HOBr concentrations remaining mostly below 0.4 ppt for the largest NO_2 concentration bin. The lack of correlation and generally much lower $BrONO_2$ in the smallest bin of < 100 ppt also indicates a potential threshold for NO_2 in a NO_x-limited regime, below which this formation pathway cannot compete (at least to produce levels above t-CIMS LOD) with the alternatives of other products that stem from the loss of BrO, e.g. HOBr in the presence of presumably abundant HO_2. This is generally supported by theory with the rate constants calculated for BLEACH23 using JPL Chemical Kinetics Evaluation number 17.[30] That for reaction 3 to produce HOBr is approximately 3.2 times the rate for reaction 9 producing $BrONO_2$. Given typical maximum HO_2 concentrations of approximately 20 ppt during the day for the MBL in Bermuda (based on work from Elshorbany et al), this would require around 60 ppt of NO_2 for $BrONO_2$ formation to become competitive with that of HO_2.[46]

Examining this relationship provides some confirmation of the current chemical mechanism where the gas phase formation of $BrONO_2$ and HOBr are both dependent on the same reactant of BrO. The dynamic relationship between these two components of Br_y is important to understand as they are known to have different photolysis lifetimes and gas-phase/heterogeneous loss pathways. Thus, changes to their respective levels in the MBL would affect the partitioning between (and the total concentrations of) gaseous inorganic bromine. Adding the layer of NO_2 concentrations demonstrates how this relationship is highly dependent on availability of limiting reactants, and can be affected by pollutant levels in marine environments. Indexing and isolating observations to even further reduce anthropogenic influence provides more evidence for pollution

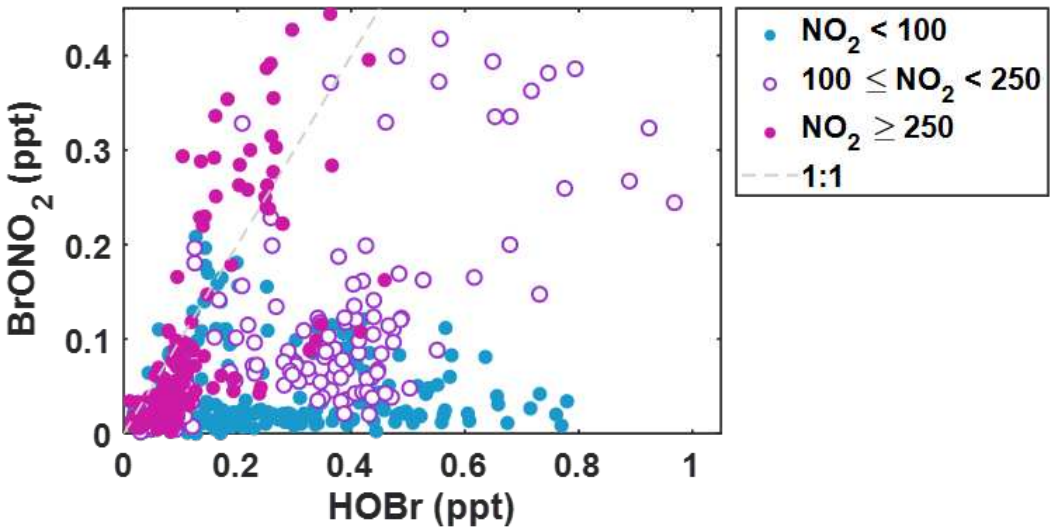

Figure 4: Scatter plot of 15-minute average concentrations for $BrONO_2$ on the y-axis and HOBr on the x-axis, colored by NO_2 concentration bins (in ppt) as measured by the LIF instrument, all reported in ppt. Filled blue circles represent data where NO_2 concentrations are below 100 ppt, open purple markers for NO_2 between 100-250 ppt, and filled magenta for concentrations above 250 ppt. Data is filtered to include only measurements during daylight hours defined as 08:00 - 16:59 local time in Bermuda.

545 driven changes and enhancements for Br^g_{y*} concentrations and is discussed in section S.4.

4 Comparison with GEOS-Chem Simulation

Shown in figure 5 are the diurnal profiles for the BLEACH23 Br^g_{y*} observations (excluding BrO) for onshore wind periods only, along with the same species and time indices from the output of the hourly GEOS-Chem simulation. Noting the difference between the y-axis ranges for both, it is clear that the GEOS-Chem
550 results generally show much higher concentrations for all Br^g_{y*} compounds compared to observations, to varying degrees for each species. For Br_2, the model for the campaign-long average overestimates observed concentrations by a factor of 2-3 and shows levels dropping to near zero during the day, presumably due to the high photolytic loss rate. When further indexing for comparison, the nighttime (19:00 - 05:59 local) Br_2 average is over a factor of 4 higher in the model compared to observations, while during daylight (8:00 - 16:59
555 local) the modeled concentrations are lower by an order of magnitude compared to observations (a factor of ∼17). BrCl shows similar behavior where its predicted levels in GEOS-Chem reduce to near zero during the day and a build up overnight (while the observations again show a significantly smaller daytime drop). The ratio of average BrCl model concentrations to observations for the campaign (again using onshore winds only) is approximately 12:1. When considering only overnight data (in the absence of photolysis), this ratio
560 increases to ∼20:1, while the daytime model mean is closer at 60% that of the observations. GEOS-Chem

also predicts nighttime BrCl concentrations to be over twice as large as those of Br_2, contrasting the t-CIMS measurements which show much lower levels and a ratio where BrCl levels are half those of Br_2.

The median HOBr concentrations show an increase coinciding with sunrise (around 07:00) for both the model and observations, the former rising more quickly to it's local maximum. The model output shows a local minimum in concentration around mid-afternoon, which is absent in the observational profile showing the largest concentrations around 10:00-12:00 for the campaign, followed by a swift decrease in signal as the sun sets (sunset times around 17:30-18:00). This bimodal shape in GEOS-Chem shows concentration maxima in the early morning hours (near 07:00) and in the evening at sunset, with residual HOBr lingering further into the nighttime hours compared to the observed trend.

$BrONO_2$ shows similar shapes in the observed and modeled profiles (especially when using all campaign data beyond onshore winds, see figure S4), where concentrations increase significantly above the nighttime near-zero background after 06:00 locally, coinciding with sunrise and the beginning of active photochemistry, with concentrations falling in the late afternoon back toward background by sunset, with a slightly larger tail into evening hours predicted by the model (as is the case with HOBr). The model also shows a characteristic drop in concentrations around midday with local maxima following at 15:00, which is somewhat captured by the measurement, though mostly below LOD in the average. This drop is presumably due to photolysis rates peaking around this time of day, which both increases the direct photolysis and loss of $BrONO_2$,[2] and impacts the NO/NO_2 ratio. Though the diel *shapes* are similar, the model once again over predicts the concentrations, in this case by nearly two orders of magnitude, where the GEOS-Chem output is approximately 75 times higher than the median level measured by the t-CIMS during the day. As these are the first in-situ observations of bromine nitrate, the similarity in the shape of the diurnal cycles between model and observations is a sign that the theoretical reactions involved in its production and loss are likely occurring in reality, while the difference in magnitude suggests that the levels of other Br_y species (e.g. BrO, with a mean daytime concentration of 0.5 ppt in the model) may be too high in the model, and/or that the rates of $BrONO_2$ formation and destruction reactions (or heterogeneous uptake) may need further sensitivity studies, at least for the MBL conditions observed at THMAO.

Diurnal profiles of NO_x, O_3, and Br_{y*}^{g} for the standard and reduced emission GEOS-Chem model outputs (along with observed trends) are shown in figure S8. Box plot distributions for each species are also shown in figures S9 and S10 to compare observed concentrations with those calculated in three different model runs (see next paragraph). The standard model simulation generally aligns well with observations of NO_x and O_3 in the campaign average, with respective mean values of 126 ppt (model) vs 83 ppt (obs) NO_2, 12 vs 10 ppt NO, and 41 vs 43 ppb O_3. Large spikes in NOx occurring over brief periods in the observations, presumably from passing ships or other local influence even when indexing for onshore winds, are generally not captured

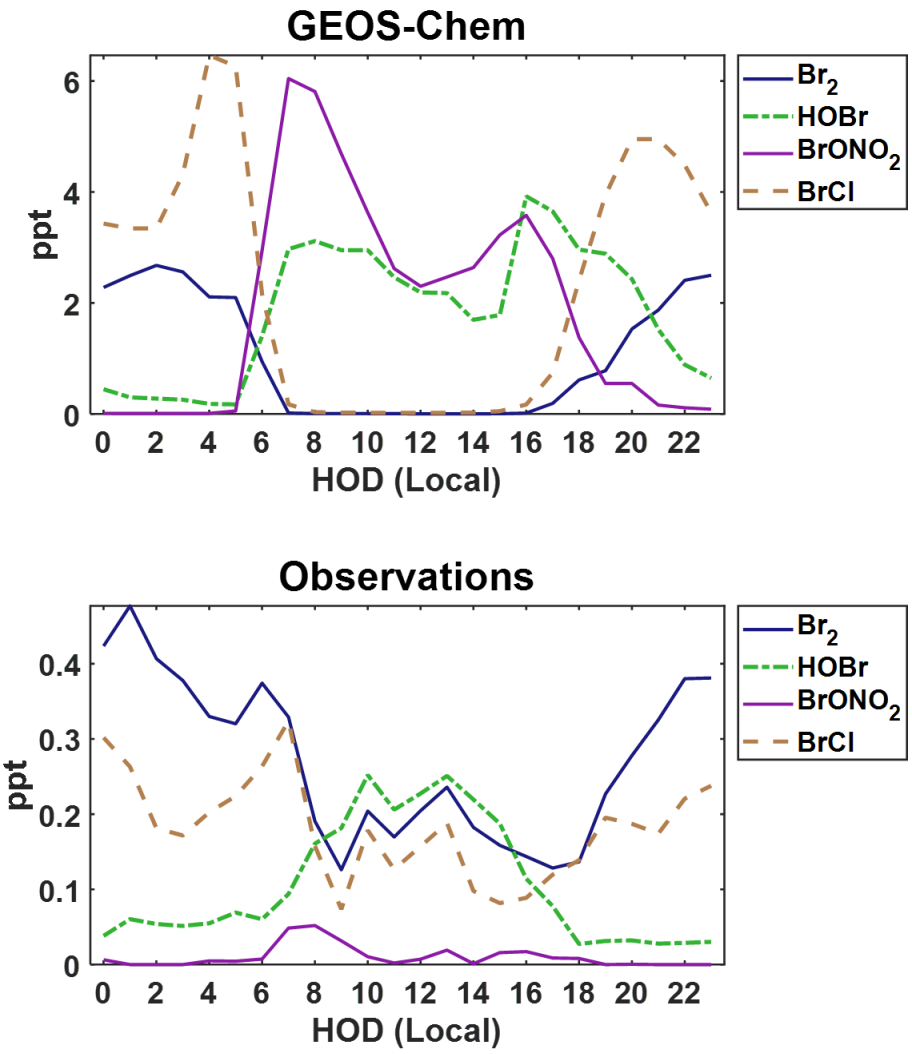

Figure 5: Diurnal profiles of Br_y species for BLEACH23 using only open ocean time periods. The top plot shows the hourly output from the GEOS-Chem simulation and the bottom displays t-CIMS concentrations for four Br_y components as presented earlier in figure 3, both of which are presented as median concentration in ppt for each (local) hourly bin. Br_2 is shown in dark blue, HOBr in green dashes, $BrONO_2$ in purple, and BrCl in brown dashes.

by the model. This is likely due to the grid resolution causing the model to treat most of the area chemically as the marine atmosphere, without much anthropogenic influence. This leads to significantly larger upper quantiles and maxima in the observed NO_x compared to the model.

Sensitivity tests to pollution were also conducted for the GEOS-Chem simulations where two additional runs were performed, the first one having global ship emissions turned off ("ShipOff"), and the second having all anthropogenic emissions excluded globally ("AnthroOff"). The same onshore wind indexing is applied in each case. Both of these simulations result in lower median NO_2, by nearly factor of 2 in the case of AnthroOff, as well as decreases in NO. The AnthroOff simulation is closest in this campaign long average to measurements of NO and NO_2. Reduction of O_3 concentrations occur in AnthroOff, but is not significant in the ShipOff scenario, while the standard model (and ShipOff) most closely resemble ozone observations. When examining the effect of less pollution on the simulated Br^g_{y*}, there is no noticeable drop in concentrations for Br_2, small decreases in $BrONO_2$ and HOBr, and significant reduction in overnight/early morning BrCl on the order of 50% for AnthroOff when compared with the standard run. This result is somewhat surprising considering the observed effect of pollution on bromine cycling discussed previously. $BrONO_2$ concentrations remain relatively close to their values in the diel trend for the standard GEOS-Chem output and over an order of magnitude larger than observed concentrations, despite significantly lower NO_2 levels. This suggests that the rate-limiting step for $BrONO_2$ formation and recycling in the model is independent of NO_2 availability, at least in the range of 50-150 ppt, contrasting the observed trend with NO_2 shown in figure 4. However, the median daytime ratio of $BrONO_2$ to HOBr does decrease in the model in the AnthroOff simulation, showing values closer to observations, as shown in figure S11.

5 Comparing Gas and Particle Phase Bromine

As established in the introduction, particle and gas-phase chemistry for halogen-containing species are intrinsically linked via heterogeneous reactions involving SSAs and potentially other aerosol species present in the MBL. It is therefore of interest to observe bromine levels in the gas *and* particle phases to gain insight into these important heterogeneous processes. In order to compare particulate and gas phase bromine in common units of mass concentration, concentrations of gaseous Br^g_{y*} species (reported thus far in units of ppt) are converted to units of μg m^{-3} of bromine using the atomic weight of 1.327e-16 μg for Br, along with temperature and pressure measurements taken concurrently with the t-CIMS at THMAO.

Summarized in figure 6 is the comparison between the GEOS-Chem simulation and observations for absolute Br mass concentrations and the relative contribution to total bromide for both the Br^g_{y*} components and the fine and coarse mode aerosol bromide. The data included in this figure are the mean (t-CIMS-

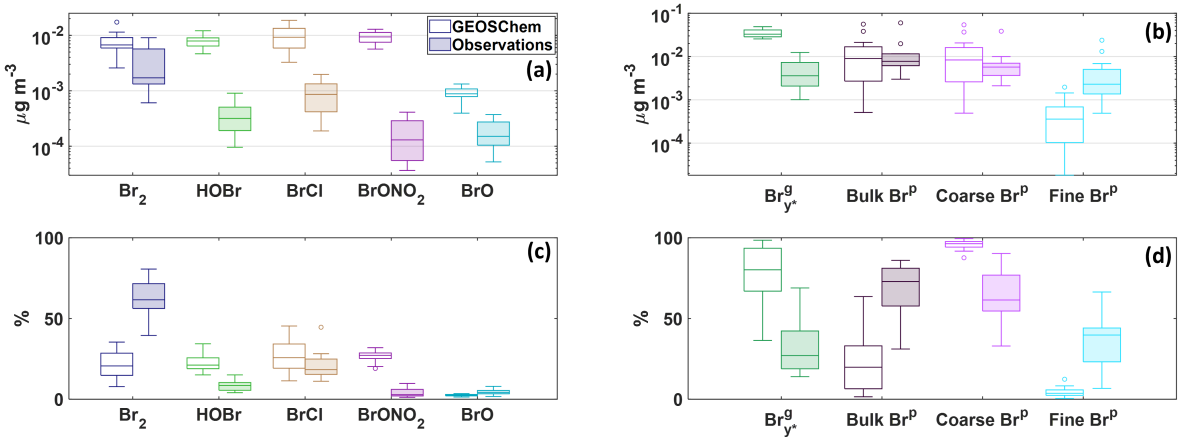

Figure 6: Box charts displaying modeled and measured absolute bromine mass concentrations. The boxes along the y-axes indicate the 25^{th} to 75^{th} percentiles (the inter-quartile range) of each variable, with the central line representing the median value. Whiskers show the minima and maxima, and outliers (calculated based on inter-quartile ranges) are shown with hollow circle markers. Model results are displayed with white boxes while observations are represented with shaded boxes. Panels (a) and (b) show the absolute mass concentration in units of μg m^{-3} on a logarithmic scale. Panels (c) and (d) display relative contributions to the corresponding total measured/modeled bromine in both the gas and particle phases (given as percentages). For panel (c), percentages are given as relative to total Br^{g}_{y*} (i.e. the sum of all 5 detected gas-phase inorganic bromine species). Values from the GEOS-Chem simulation are shown with unfilled white boxes, while measurements from the t-CIMS and aerosol filters are shown with filled color boxes.

measured) Br^{g}_{y*} mass concentrations during the time period of all filter measurements where the t-CIMS was concurrently operational. This leads to the inclusion of 16 filter periods, most of which have a sampling duration of ~24 hours. Because of the coarser time resolution, filter measurements cannot be indexed to only include onshore winds. We therefore include the mean concentration of *all* viable t-CIMS Br^{g}_{y*} measurements for this analysis. Total Br^{g}_{y*} is represented in green for the panels (b) and (d), which also include the total or "bulk" particle-phase bromide mass, as well as two individual size bins designated as 'fine' ($< 0.9\ \mu m$) and 'coarse' mode ($\geq 0.9\ \mu m$), based on the values for the aerodynamic size bins of the cascade impactor measurements to be comparable with fine and course mode designations in the GEOS-Chem model. The relative contributions for fine and coarse mode bromide (%) shown in panel (d) are calculated by dividing their mass concentrations by that of the bulk aerosol bromide (sum over all sizes). Br^{g}_{y*} and bulk particulate bromide (Br^{p}) are shown in green and dark purple, respectively, as their relative contributions to the sum of both. This shows the relative gas-phase and particle-phase fraction of total detectable atmospheric bromine at THMAO (noting the absence of some gas-phase Br_y components).

Figures 6 and 5 show a clear over-prediction in the GEOS-Chem simulation of total Br^{g}_{y*} as well as it's individual components, now contextualized with the particle phase. The total Br^{g}_{y*} mass concentration is significantly higher in the model output, by an order of magnitude when comparing the median values

from GEOS-Chem against that of the observations. The total (bulk) Br^p mass is captured fairly well in the simulation, showing similar median concentration to the measured values. However, when looking at the size-resolved comparison, the model underestimates the median bromide mass in fine-mode particles by nearly an order of magnitude. The relative contribution to total measurable Br mass also shows discrepancies, where the model predicts more of the total mass to be in the gas phase (Br^g_{y*}) with a median of 80% while observations show a median of 27%, with the remaining fraction in the particle phase. The discrepancy between the model and observations for fine mode Br^p alone with a median difference of 0.2e-2 $\mu g\ m^{-3}$ is not enough to account for the much larger difference of 2.9e-2 $\mu g\ m^{-3}$ between the modeled and observed Br^g_{y*} median concentrations. Total measured bromide (gas + particle phases) is higher in the model by over a factor of 3 comparing the median mass concentrations from figure 6.

The lack of measurements for all Br^g_y species leaves the potential for a reservoir species to explain such a large difference in gas-phase mass, e.g. hydrogen bromide (HBr) and free atomic bromine, Br. CIMS measurements using iodide as a reagent have been reported to be over 100 times less sensitive to HBr compared to Br_2.[59] In the case of the t-IMR at THMAO, this would mean that the LOD for HBr would be 2 orders of magnitude higher, which when applied to its spectral neighbor, HOBr, would mean concentrations less than the order of 10 ppt would not be detectable in the observations. GEOS-Chem predicts HBr concentrations to peak at approximately 3 ppt at midday from the median diurnal profile. We therefore consider this Br^g_{y*} as a lower limit to the actual total gaseous bromine mass. Though even with this caveat, there remain large differences between the GEOS-Chem output and observations for the fractional contribution of Br^g_{y*} components to total Br^g_y.

Mass concentrations of other particulate species measured at THMAO are shown in figure 7 along with the values modeled in the GEOS-Chem simulation. Analogous to figure 6, observations are again shown in shaded boxes with whiskers extending to the maximum and minimum (outliers in open circles), with log scale on the y-axis for all panels. Fine mode sodium (Na^p) and chloride (Cl^p) are both underestimated in the model output, the latter by a much larger factor. Bulk Na^p and Cl^p concentrations show similar medians and spreads between GEOS-Chem and the observed, with coarse mode for both also within uncertainties. Particulate sulfate and nitrate are relatively close to observed values in the model output across both size bins and consequently in the bulk mass concentrations, with a small difference noted between the medians of fine sulfate. Modeled iodine concentrations in the particle phase (I^p) are underestimated in both the fine and coarse modes compared to the filter measurements. The underestimation of fine Na^p has the potential of contributing to the fine mode halide differences to some degree. However, the sea-salt production mechanism in GEOS-Chem is relatively simple, and the difference in the fine mode is much smaller than the magnitude of the coarse and bulk Na^p concentrations, which are mostly in agreement. While the bulk mass of sea salt

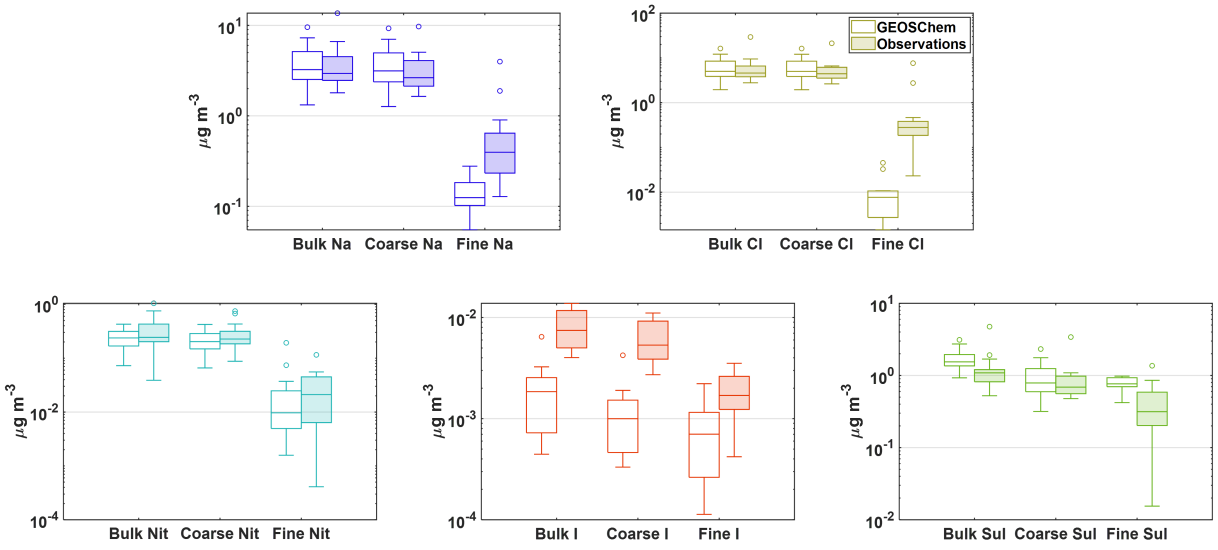

Figure 7: Box charts displaying modeled and measured absolute mass concentrations of other species detected from the filters at THMAO. Values shown with a log-scale y axis in units of μg m^{-3} for particulate sodium (Na, blue), chlorine (Cl, yellow), nitrate (Nit, cyan), iodine (I, red), and sulfate (Sul, green) content. Values from the GEOS-Chem simulation are shown with unfilled white boxes, while measurements from the t-CIMS and aerosol filters are shown with filled color boxes.

alone cannot explain the observed differences in Br_y, the size distribution and thus available surface area may be another source of discrepancy. Fine mode aerosol halide mass concentrations, Br^p, Cl^p, and I^p, all being measured at concentrations much larger than predicted in the model by varying magnitudes, and all larger than that of Na^p also suggests that either the uptake rate of halogenated molecules onto smaller particles is underestimated, or that the conversion of aqueous halogen species in fine mode aerosol back to the gas phase is too efficient in the model simulation.

There is clearly much uncertainty remaining in the various processes and rates at which reactive bromine (and other halogens) is recycled, especially in regards to heterogeneous chemistry with SSAs and potentially OA as well. Identifying the main sources/sinks of observed gaseous and particulate bromide in the marine atmosphere will help add constraints to models with highly uncertain parameters and improve our understanding of the impact of MBL Br chemistry on the global atmospheric composition.

6 Conclusions

With this work we have confirmed the identities and made simultaneous measurements of five key gas-phase inorganic bromine species (Br_2, BrCl, HOBr, $BrONO_2$, and BrO) in the semi-remote MBL with the t-CIMS. This includes (to our knowledge) the first in-situ observations of bromine nitrate, $BrONO_2$. Direct calibration for Br_2, along with laboratory experiments to calibrate for HOBr, reinforce the use of binding

enthalpy calculations to extrapolate and determine sensitivities for all species measured during the BLEACH campaign, along with a detailed humidity-based sensitivity correction of Br_2.

Online measurements were made for multiple weeks at THMAO, which experienced a multitude of atmospheric conditions in the MBL, ranging from marine sourced air masses mostly uninfluenced by anthropogenic activity, to highly localized (and occasionally continentally transported) polluted regimes. We find that the measured HOBr and $BrONO_2$ align qualitatively with current understandings of gas-phase Br_y formation and loss pathways, especially when considering the influence of NO_x concentrations from long range transport, passing ships, and local anthropogenic sources present near the sampling site. Br_2 and BrCl show unexpectedly high (or rather lack of a decrease in) concentrations during the day, where photolytic loss has been assumed to dominate and outpace their formation in the natural MBL. This behavior is determined to be beyond systematic inlet conversion and is attributed to either an unknown local source of bromine, enhanced heterogeneous cycling due to higher NO_x and nitrate chemistry, or some combination of both.

The observations of Br^g_{y*} at THMAO are compared with concentrations produced by a GEOS-Chem model simulation output for the grid box containing Bermuda. The model is run with the most recent standard halogen chemistry module, which includes the acid-catalyzed debromination of sea salt aerosols (SSAs). Results show that both the total Br^g_{y*} and the concentration of each individual species are significantly higher in the model, by over an order of magnitude in multiple cases. The largest overestimate by the model is for bromine nitrate ($BrONO_2$). Additional model runs with both ship emissions and all anthropogenic emissions turned off, do not show a significant drop in $BrONO_2$ or total Br^g_{y*} toward their observed levels, despite NO_x and O_3 being reduced by approximately a factor of 2 in the latter case. This indicates that the model production of bromine nitrate (and further partitioning among Br_y components) is not very sensitive to NO_x and ozone levels, at least at respective concentrations on the order of 200 ppt and 40 ppb, contrasting observations which show a clear dependence of $BrONO_2$ concentrations on NO_2.

Aerosol filter measurements taken at THMAO also give insight into multiphase reactive bromine chemistry. The GEOS-Chem simulation overestimates the fraction of total atmospheric bromide in the gas phase, thereby underestimating the fraction in the particle phase. The model also underestimates fine-mode particle concentrations of chlorine, bromine, and iodine. The observed particle composition indicates an unaccounted for source of halogens in the MBL for the coastal site and/or the need to adjust reaction rates and partitioning as it is understood in the model.

The work presented here demonstrates several methods of quality control for the first field deployment and in-situ measurements from the t-IMR, and establishes observational constraints for a large fraction of inorganic Br_y species in the sub-tropical MBL. The five observed components of reactive bromine presented in this work have not been previously reported to be simultaneously measured in-situ above detection limits.

These first observations of $BrONO_2$ specifically have allowed for investigation into effects of pollutant levels on Br_y, as well as provide insights into heterogeneous cycling in the marine atmosphere. Coordinated observations from multiple instruments as part of the BLEACH campaign have made possible a more detailed examination of gas and particle phase partitioning, while model comparisons point out the potential for future improvements in our understanding of the bromine (and overall halogen) chemical mechanism in the atmosphere. Changing the rates of these simulated reactions in the MBL to better reflect observations has the potential to significantly alter our understanding of the total oxidative capacity of the atmosphere and trace pollutant concentrations.

References

[1] William R. Simpson et al. "Tropospheric Halogen Chemistry: Sources, Cycling, and Impacts". In: *Chemical Reviews* 115 (10 May 2015), pp. 4035–4062. ISSN: 0009-2665. DOI: 10.1021/cr5006638.

[2] J. Liao et al. "Observations of inorganic bromine (HOBr, BrO, and Br ¡sub¿2¡/sub¿) speciation at Barrow, Alaska, in spring 2009". In: *Journal of Geophysical Research: Atmospheres* 117 (D14 July 2012). ISSN: 0148-0227. DOI: 10.1029/2011JD016641.

[3] W. R. Simpson et al. "Halogens and their role in polar boundary-layer ozone depletion". In: *Atmospheric Chemistry and Physics* 7 (16 Aug. 2007), pp. 4375–4418. ISSN: 1680-7324. DOI: 10.5194/acp-7-4375-2007.

[4] Siyuan Wang et al. "Direct detection of atmospheric atomic bromine leading to mercury and ozone depletion". In: *Proceedings of the National Academy of Sciences* 116 (29 July 2019), pp. 14479–14484. ISSN: 0027-8424. DOI: 10.1073/pnas.1900613116.

[5] Tao Wang et al. "Ozone pollution in China: A review of concentrations, meteorological influences, chemical precursors, and effects". In: *Science of The Total Environment* 575 (Jan. 2017), pp. 1582–1596. ISSN: 00489697. DOI: 10.1016/j.scitotenv.2016.10.081.

[6] Qinyi Li et al. "Reactive halogens increase the global methane lifetime and radiative forcing in the 21st century". In: *Nature Communications* 13 (1 May 2022), p. 2768. ISSN: 2041-1723. DOI: 10.1038/s41467-022-30456-8.

[7] A. S. Mahajan et al. "Measurement and modelling of tropospheric reactive halogen species over the tropical Atlantic Ocean". In: *Atmospheric Chemistry and Physics* 10 (10 May 2010), pp. 4611–4624. ISSN: 1680-7324. DOI: 10.5194/acp-10-4611-2010.

[8] W. J. Bloss et al. "Impact of halogen monoxide chemistry upon boundary layer OH and HO_2 concentrations at a coastal site". In: *Geophysical Research Letters* 32 (6 Mar. 2005). ISSN: 0094-8276. DOI: 10.1029/2004GL022084.

[9] Hans D. Osthoff et al. "High levels of nitryl chloride in the polluted subtropical marine boundary layer". In: *Nature Geoscience* 1 (5 May 2008), pp. 324–328. ISSN: 1752-0894. DOI: 10.1038/ngeo177.

[10] Cameron Faxon, Jeffrey Bean, and Lea Ruiz. "Inland Concentrations of Cl2 and ClNO2 in Southeast Texas Suggest Chlorine Chemistry Significantly Contributes to Atmospheric Reactivity". In: *Atmosphere* 6 (10 Oct. 2015), pp. 1487–1506. ISSN: 2073-4433. DOI: 10.3390/atmos6101487.

[11] Ben H. Lee et al. "Flight Deployment of a High-Resolution Time-of-Flight Chemical Ionization Mass Spectrometer: Observations of Reactive Halogen and Nitrogen Oxide Species". In: *Journal of Geophysical Research: Atmospheres* 123 (14 July 2018), pp. 7670–7686. ISSN: 2169-897X. DOI: 10.1029/2017JD028082.

[12] Alfonso Saiz-Lopez et al. "Nighttime atmospheric chemistry of iodine". In: *Atmospheric Chemistry and Physics* 16 (24 Dec. 2016), pp. 15593–15604. ISSN: 1680-7324. DOI: 10.5194/acp-16-15593-2016.

[13] Deanna L. Donohoue et al. "Temperature and Pressure Dependent Rate Coefficients for the Reaction of Hg with Br and the Reaction of Br with Br: A Pulsed Laser Photolysis-Pulsed Laser Induced Fluorescence Study". In: *The Journal of Physical Chemistry A* 110 (21 June 2006), pp. 6623–6632. ISSN: 1089-5639. DOI: 10.1021/jp054688j.

[14] Itsaso Auzmendi-Murua and Joseph W. Bozzelli. "Gas Phase Mercury Oxidation by Halogens (Cl, Br, I) in Combustion Effluents: Influence of Operating Conditions". In: *Energy Fuels* 30 (1 Jan. 2016), pp. 603–615. ISSN: 0887-0624. DOI: 10.1021/acs.energyfuels.5b01958.

[15] P. S. Monks et al. "Tropospheric ozone and its precursors from the urban to the global scale from air quality to short-lived climate forcer". In: *Atmospheric Chemistry and Physics* 15 (15 Aug. 2015), pp. 8889–8973. ISSN: 1680-7324. DOI: 10.5194/acp-15-8889-2015.

[16] Chelsea R. Stephens et al. "The relative importance of chlorine and bromine radicals in the oxidation of atmospheric mercury at Barrow, Alaska". In: *Journal of Geophysical Research: Atmospheres* 117 (D14 July 2012). ISSN: 0148-0227. DOI: 10.1029/2011JD016649.

[17] Katie A. Read et al. "Author Correction: Extensive halogen-mediated ozone destruction over the tropical Atlantic Ocean". In: *Nature* 631 (8019 July 2024), E5–E5. ISSN: 0028-0836. DOI: 10.1038/s41586-024-07649-w.

[18] H. Grythe et al. "A review of sea-spray aerosol source functions using a large global set of sea salt aerosol concentration measurements". In: *Atmospheric Chemistry and Physics* 14 (3 Feb. 2014), pp. 1277–1297. ISSN: 1680-7324. DOI: 10.5194/acp-14-1277-2014.

[19] L. Jaeglé et al. "Global distribution of sea salt aerosols: new constraints from in situ and remote sensing observations". In: *Atmospheric Chemistry and Physics* 11 (7 Apr. 2011), pp. 3137–3157. ISSN: 1680-7324. DOI: 10.5194/acp-11-3137-2011.

[20] Timothy H. Bertram et al. "Sea spray aerosol chemical composition: elemental and molecular mimics for laboratory studies of heterogeneous and multiphase reactions". In: *Chemical Society Reviews* 47 (7 2018), pp. 2374–2400. ISSN: 0306-0012. DOI: 10.1039/C7CS00008A.

[21] Rainer Vogt, Paul J. Crutzen, and Rolf Sander. "A mechanism for halogen release from sea-salt aerosol in the remote marine boundary layer". In: *Nature* 383 (6598 Sept. 1996), pp. 327–330. ISSN: 0028-0836. DOI: 10.1038/383327a0.

[22] Alfonso Saiz-Lopez and John M. C. Plane. "Novel iodine chemistry in the marine boundary layer". In: *Geophysical Research Letters* 31 (4 Feb. 2004). ISSN: 0094-8276. DOI: 10.1029/2003GL019215.

[23] Dexian Chen et al. "Airborne measurements of BrO and the sum of HOBr and Br_2 over the tropical west pacific from 1 to 15km during the convective transport of active species in the tropics (CONTRAST) experiment". In: *Journal of Geophysical Research* 121 (20 2016). ISSN: 21562202. DOI: 10.1002/2016JD025561.

[24] Michael Le Breton et al. "Enhanced ozone loss by active inorganic bromine chemistry in the tropical troposphere". In: *Atmospheric Environment* 155 (Apr. 2017), pp. 21–28. ISSN: 13522310. DOI: 10.1016/j.atmosenv.2017.02.003.

[25] Xuan Wang et al. "Global tropospheric halogen (Cl, Br, I) chemistry and its impact on oxidants". In: *Atmospheric Chemistry and Physics* 21 (18 Sept. 2021), pp. 13973–13996. ISSN: 1680-7324. DOI: 10.5194/acp-21-13973-2021.

[26] R. von Glasow et al. "Impact of reactive bromine chemistry in the troposphere". In: *Atmospheric Chemistry and Physics* 4 (11/12 Dec. 2004), pp. 2481–2497. ISSN: 1680-7324. DOI: 10.5194/acp-4-2481-2004.

[27] Shuting Zhai et al. "Anthropogenic Influence on Tropospheric Reactive Bromine Since the Pre-industrial: Implications for Arctic Ice-Core Bromine Trends". In: *Geophysical Research Letters* 51 (5 Mar. 2024). ISSN: 0094-8276. DOI: 10.1029/2023GL107733.

[28] Alfonso Saiz-Lopez and Roland von Glasow. "Reactive halogen chemistry in the troposphere". In: *Chemical Society Reviews* 41 (19 2012), p. 6448. ISSN: 0306-0012. DOI: 10.1039/c2cs35208g.

[29] N. Bobrowski et al. "Detection of bromine monoxide in a volcanic plume". In: *Nature* 423 (6937 May 2003), pp. 273–276. ISSN: 0028-0836. DOI: 10.1038/nature01625.

[30] S P Sander et al. *Chemical Kinetics and Photochemical Data for Use in Atmospheric Studies, Evaluation No. 17*. Feb. 2011.

[31] Peng Zhang et al. "The influence of a single water molecule on the reaction of BrO + HO2". In: *Scientific Reports* 13 (1 Aug. 2023), p. 13014. ISSN: 2045-2322. DOI: 10.1038/s41598-023-28783-x.

[32] U. Hausmann M. Platt. "Spectroscopic measurement of bromine oxide and ozone in the high Arctic during Polar Sunrise Experiment 1992". In: *Journal of Geophysical Research: Atmospheres* 99 (D12 Dec. 1994), pp. 25399–25413. ISSN: 0148-0227. DOI: 10.1029/94JD01314.

[33] J. A. Neuman et al. "Bromine measurements in ozone depleted air over the Arctic Ocean". In: *Atmospheric Chemistry and Physics* 10 (14 July 2010), pp. 6503–6514. ISSN: 1680-7324. DOI: 10.5194/acp-10-6503-2010.

[34] Joelle Buxmann et al. "Consumption of reactive halogen species from sea-salt aerosol by secondary organic aerosol: slowing down the bromine explosion". In: *Environmental Chemistry* 12 (4 2015), p. 476. ISSN: 1448-2517. DOI: 10.1071/EN14226.

[35] Johannes Ofner et al. "Halogen-induced organic aerosol (XOA): a study on ultra-fine particle formation and time-resolved chemical characterization". In: *Faraday Discussions* 165 (2013), p. 135. ISSN: 1359-6640. DOI: 10.1039/c3fd00093a.

[36] Masao Gen et al. "Particulate nitrate photolysis in the atmosphere". In: *Environmental Science: Atmospheres* 2 (2 2022), pp. 111–127. ISSN: 2634-3606. DOI: 10.1039/D1EA00087J.

[37] B. D. Finley and E. S. Saltzman. "Observations of Cl_2, Br_2, and I_2 in coastal marine air". In: *Journal of Geophysical Research: Atmospheres* 113 (D21 Nov. 2008). ISSN: 0148-0227. DOI: 10.1029/2008JD010269.

[38] Shanshan Wang et al. "Typhoon- and pollution-driven enhancement of reactive bromine in the mid-latitude marine boundary layer". In: *National Science Review* 11 (4 Feb. 2024). ISSN: 2095-5138. DOI: 10.1093/nsr/nwae074.

[39] Men Xia et al. "Pollution-Derived Br_2 Boosts Oxidation Power of the Coastal Atmosphere". In: *Environmental Science Technology* 56 (17 Sept. 2022), pp. 12055–12065. ISSN: 0013-936X. DOI: 10.1021/acs.est.2c02434.

[40] Anoop S. Mahajan et al. "High bromine oxide concentrations in the semi-polluted boundary layer". In: *Atmospheric Environment* 43 (25 Aug. 2009), pp. 3811–3818. ISSN: 13522310. DOI: 10.1016/j.atmosenv.2009.05.033.

[41] Ulrich Platt and Christof Janssen. "Observation and role of the free radicals NO3, ClO, BrO and IO in the troposphere". In: *Faraday Discussions* 100 (1995), p. 175. ISSN: 1359-6640. DOI: 10.1039/fd9950000175.

[42] Phil Rund et al. "Laboratory and field characterization of an atmospheric pressure transverse chemical ionization ion-molecule reaction region". In: *Atmospheric Measurement Techniques* 18 (22 Nov. 2025), pp. 6979–6995. ISSN: 1867-8548. DOI: 10.5194/amt-18-6979-2025.

[43] Yuting Zhu et al. "An investigation into the chemistry of HONO in the marine boundary layer at Tudor Hill Marine Atmospheric Observatory in Bermuda". In: *Atmospheric Chemistry and Physics* 22 (9 May 2022), pp. 6327–6346. ISSN: 1680-7324. DOI: 10.5194/acp-22-6327-2022.

[44] Youfeng Wang et al. "Observational Evidence of Unknown NO x Source and Its Perturbation of Oxidative Capacity in Bermuda's Marine Boundary Layer". In: *Journal of Geophysical Research: Atmospheres* 128 (24 Dec. 2023). ISSN: 2169-897X. DOI: 10.1029/2023JD039582.

[45] Patrick Boylan, Detlev Helmig, and Samuel Oltmans. "Ozone in the Atlantic Ocean marine boundary layer". In: *Elementa: Science of the Anthropocene* 3 (Jan. 2015). ISSN: 2325-1026. DOI: 10.12952/journal.elementa.000045.

[46] Yasin Elshorbany et al. "Seasonal dependency of the atmospheric oxidizing capacity of the marine boundary layer of Bermuda". In: *Atmospheric Environment* 289 (Nov. 2022), p. 119326. ISSN: 13522310. DOI: 10.1016/j.atmosenv.2022.119326.

[47] Andrew W. Rollins et al. "Single-photon laser-induced fluorescence detection of nitric oxide at sub-parts-per-trillion mixing ratios". In: *Atmospheric Measurement Techniques* 13 (5 May 2020), pp. 2425–2439. ISSN: 1867-8548. DOI: 10.5194/amt-13-2425-2020.

[48] T. H. Bertram et al. "A field-deployable, chemical ionization time-of-flight mass spectrometer". In: *Atmospheric Measurement Techniques* 4 (7 July 2011), pp. 1471–1479. ISSN: 1867-8548. DOI: 10.5194/amt-4-1471-2011.

[49] Siddharth Iyer et al. "Modeling the Detection of Organic and Inorganic Compounds Using Iodide-Based Chemical Ionization". In: *The Journal of Physical Chemistry A* 120 (4 Feb. 2016), pp. 576–587. ISSN: 1089-5639. DOI: 10.1021/acs.jpca.5b09837.

[50] John P. Perdew, Kieron Burke, and Matthias Ernzerhof. "Generalized Gradient Approximation Made Simple". In: *Physical Review Letters* 77 (18 Oct. 1996), pp. 3865–3868. ISSN: 0031-9007. DOI: 10.1103/PhysRevLett.77.3865.

[51] Rick A. Kendall, Thom H. Dunning, and Robert J. Harrison. "Electron affinities of the first-row atoms revisited. Systematic basis sets and wave functions". In: *The Journal of Chemical Physics* 96 (9 May 1992), pp. 6796–6806. ISSN: 0021-9606. DOI: 10.1063/1.462569.

[52] M. J. Frisch et al. *Gaussian˜16 Revision C.01*. Gaussian Inc. Wallingford CT. 2016.

[53] David Feller. "The Role of Databases in Support of Computational Chemistry Calculations". In: *Journal of Computational Chemistry* 17 (13 1996), pp. 1571–1586.

[54] Kirk A. Peterson et al. "Systematically convergent basis sets with relativistic pseudopotentials. II. Small-core pseudopotentials and correlation consistent basis sets for the post- d group 16–18 elements". In: *The Journal of Chemical Physics* 119 (21 Dec. 2003), pp. 11113–11123. ISSN: 0021-9606. DOI: 10.1063/1.1622924.

[55] Christoph Riplinger et al. "Natural triple excitations in local coupled cluster calculations with pair natural orbitals". In: *The Journal of Chemical Physics* 139 (13 Oct. 2013). ISSN: 0021-9606. DOI: 10.1063/1.4821834.

[56] Christoph Riplinger and Frank Neese. "An efficient and near linear scaling pair natural orbital based local coupled cluster method". In: *The Journal of Chemical Physics* 138 (3 Jan. 2013). ISSN: 0021-9606. DOI: 10.1063/1.4773581.

[57] Florian Weigend and Reinhart Ahlrichs. "Balanced basis sets of split valence, triple zeta valence and quadruple zeta valence quality for H to Rn: Design and assessment of accuracy". In: *Physical Chemistry Chemical Physics* 7 (18 2005), p. 3297. ISSN: 1463-9076. DOI: 10.1039/b508541a.

[58] Frank Neese. "The ORCA program system". In: *WIREs Computational Molecular Science* 2 (1 Jan. 2012), pp. 73–78. ISSN: 1759-0876. DOI: 10.1002/wcms.81.

[59] J. Liao et al. "Characterization of soluble bromide measurements and a case study of BrO observations during ARCTAS". In: *Atmospheric Chemistry and Physics* 12 (3 Feb. 2012), pp. 1327–1338. ISSN: 1680-7324. DOI: 10.5194/acp-12-1327-2012.

[60] Jordan Krechmer et al. "Evaluation of a New Reagent-Ion Source and Focusing Ion–Molecule Reactor for Use in Proton-Transfer-Reaction Mass Spectrometry". In: *Analytical Chemistry* 90 (20 Oct. 2018), pp. 12011–12018. ISSN: 0003-2700. DOI: 10.1021/acs.analchem.8b02641.

[61] J. P. Kercher, T. P. Riedel, and J. A. Thornton. "Chlorine activation by N_2O_5: simultaneous, in situ detection of $ClNO_2$ by chemical ionization mass spectrometry". In: *Atmospheric Measurement Techniques* 2 (1 May 2009), pp. 193–204. ISSN: 1867-8548. DOI: 10.5194/amt-2-193-2009.

[62] Raphael Dörich et al. "Iodide CIMS and m / z 62: the detection of HNO_3 as NO_3^- in the presence of PAN, peroxyacetic acid and ozone". In: *Atmospheric Measurement Techniques* 14 (8 Aug. 2021), pp. 5319–5332. ISSN: 1867-8548. DOI: 10.5194/amt-14-5319-2021.

[63] Alexander Zaytsev et al. "Using collision-induced dissociation to constrain sensitivity of ammonia chemical ionization mass spectrometry (NH_4^+ CIMS) to oxygenated volatile organic compounds". In: *Atmospheric Measurement Techniques* 12 (3 Mar. 2019), pp. 1861–1870. ISSN: 1867-8548. DOI: 10.5194/amt-12-1861-2019.

[64] Yury Minenkov et al. "Heats of Formation of Medium-Sized Organic Compounds from Contemporary Electronic Structure Methods". In: *Journal of Chemical Theory and Computation* 13 (8 Aug. 2017), pp. 3537–3560. ISSN: 1549-9618. DOI: 10.1021/acs.jctc.7b00335.

[65] Tomás Sherwen et al. "Global impacts of tropospheric halogens (Cl, Br, I) on oxidants and composition in GEOS-Chem". In: *Atmospheric Chemistry and Physics* 16 (18 Sept. 2016), pp. 12239–12271. ISSN: 1680-7324. DOI: 10.5194/acp-16-12239-2016.

[66] Q. Chen et al. "Sulfate production by reactive bromine: Implications for the global sulfur and reactive bromine budgets". In: *Geophysical Research Letters* 44 (13 July 2017), pp. 7069–7078. ISSN: 0094-8276. DOI: 10.1002/2017GL073812.

[67] Bermuda Electric Light Company Limited. *BELCO Power Supply Explained*. URL: https://belco.bm/belco-power-supply-explained/.

[68] Y.K. Kharaka and J.S. Hanor. "Deep Fluids in Sedimentary Basins". In: Elsevier, 2014, pp. 471–515. DOI: 10.1016/B978-0-08-095975-7.00516-7.

[69] Orfan Shouakar-Stash, Robert J. Drimmie, and Shaun K. Frape. "Determination of inorganic chlorine stable isotopes by continuous flow isotope ratio mass spectrometry". In: *Rapid Communications in Mass Spectrometry* 19 (2 Jan. 2005), pp. 121–127. ISSN: 0951-4198. DOI: 10.1002/rcm.1762.

[70] J. Liao et al. "A comparison of Arctic BrO measurements by chemical ionization mass spectrometry and long path-differential optical absorption spectroscopy". In: *Journal of Geophysical Research* 116 (Jan. 2011), D00R02. ISSN: 0148-0227. DOI: 10.1029/2010JD014788.

[71] A. F. Stein et al. "NOAA's HYSPLIT Atmospheric Transport and Dispersion Modeling System". In: *Bulletin of the American Meteorological Society* 96 (12 Dec. 2015), pp. 2059–2077. ISSN: 0003-0007. DOI: 10.1175/BAMS-D-14-00110.1.

[72] Louis Marelle et al. "Implementation and Impacts of Surface and Blowing Snow Sources of Arctic Bromine Activation Within WRF Chem 4.1.1". In: *Journal of Advances in Modeling Earth Systems* 13 (8 Aug. 2021). ISSN: 1942-2466. DOI: 10.1029/2020MS002391.

[73] T. J. Roberts et al. “Re-evaluating the reactive uptake of HOBr in the troposphere with implications for the marine boundary layer and volcanic plumes”. In: *Atmospheric Chemistry and Physics* 14 (20 Oct. 2014), pp. 11185–11199. ISSN: 1680-7324. DOI: 10.5194/acp-14-11185-2014.

[74] Pascal Pratte and Michel J. Rossi. “The heterogeneous kinetics of HOBr and HOCl on acidified sea salt and model aerosol at 40-90% relative humidity and ambient temperature”. In: *Phys. Chem. Chem. Phys.* 8 (34 2006), pp. 3988–4001. ISSN: 1463-9076. DOI: 10.1039/B604321F.

[75] Paul Nissenson et al. “Rapid formation of molecular bromine from deliquesced NaBr aerosol in the presence of ozone and UV light”. In: *Atmospheric Environment* 89 (June 2014), pp. 491–506. ISSN: 13522310. DOI: 10.1016/j.atmosenv.2014.02.056.

[76] D Jacob. “Heterogeneous chemistry and tropospheric ozone”. In: *Atmospheric Environment* 34 (12-14 2000), pp. 2131–2159. ISSN: 13522310. DOI: 10.1016/S1352-2310(99)00462-8.

[77] M. J. Tang, R. A. Cox, and M. Kalberer. “Compilation and evaluation of gas phase diffusion coefficients of reactive trace gases in the atmosphere: volume 1. Inorganic compounds”. In: *Atmospheric Chemistry and Physics* 14 (17 Sept. 2014), pp. 9233–9247. ISSN: 1680-7324. DOI: 10.5194/acp-14-9233-2014.

Supplemental Materials

S.1 Spectral Identification of Br^{g}_{y*} Components

Bromine atoms have two naturally occurring stable isotopes at weights of 79 and 81 amu, which occur approximately in equal abundance: Br^{79} with 50.7% and Br^{81} with 49.3%.[68] Chlorine atoms also have two stable isotopes: Cl^{35} with relative abundance of 75.8% and Cl^{37} with 24.2%.[69] This creates distinct signatures in a mass spectrum for both elements and all compounds that contain them, where a 1:1 ratio is expected for clusters containing one bromine atom at base mass to charge ratio m and the corresponding isotope peak at $m+2$. Meanwhile an approximate 3:1 ratio is expected for single chlorine-containing species, also for peaks at m/Q m and $m+2$, respectively.

With ambient atmospheric mass spectrometry, it is common to observe multiple species peaks at the same unit mass, with the possibility of interference between multiple molecules close in mass-to-charge values, depending on resolution. However, halogenated species, including both the bromine and chlorine-containing molecules discussed here as well as iodine (i.e. the reagent ion used here), show a negative mass defect in measured spectra. This means that the exact m/Q position for a halogenated peak is more negative compared to other species, i.e. organic clusters for which iodide mode CIMS is sensitive. This, combined with the high resolving power of the LToF CIMS, separates the peak m/Q position of bromine-containing molecules (clustered to I^-), decreasing the likelihood of interference from overlapping clusters compared with other ambient compounds detected, typically making their identification relatively more robust.

Figure S1 shows representative spectra for an ambient sampling period during the BLEACH campaign for the main bromine containing compounds presented in this work. Baseline-subtracted spectra as ion counts (per m/Q bin) as measured by the t-CIMS are displayed in the red traces for each plot, while green bars show the exact m/Q position and initial fitted peak height for each compound when clustered with the reagent I^-, labeled in green above the corresponding first isotope peak. Isotope ratio patterns of 1:1 are clear for the clusters $BrOI^-$ and $HOBrI^-$ consistent with the single bromine atom in each. For the $BrONO_2I^-$ cluster, the heavier isotope peak at approximate m/Q 269.8 is dwarfed by the peak for I_2O^-, an instrument artifact from iodide reagent chemistry, which is consistently larger throughout sampling. However, the large mass defect and high resolution for the first isotope peak at m/Q 267.8 support the identification of this detected species. Diatomic bromine with a first peak at m/Q 284.74 shows a consistent isotopic pattern of approximately 1:2:1 at masses $m+2$ and $m+4$, resulting from the four possible combinations of Br^{79} and Br^{81}. The combination of bromine and chlorine atoms for the $BrClI^-$ also shows an isotopic peak signature consistent with expectation (i.e. the magnitude of the green bars). Save for the one exception with a larger

peak overlap, the combination of high mass resolving power, negative mass defect for halogenated sample molecules, and the distinct isotope signature for Br and Cl atoms confirms the spectral identification of these
985 measured bromine-containing molecules in ambient sampling throughout the campaign.

S.2 Aerosol Measurements

Table S1: Mean aerosol concentrations and propagated error during BLEACH.

[a] Mean concentration ± mean propagated error

[b] Fine mode refers to particles < 0.9 μm in aerodynamic diameter

[c] Coarse mode refers to particles ≥ 0.9 μm in aerodynamic diameter

Type	**Chloride** ($\mu g\ m^{-3}$)	**Bromide** ($\mu g\ m^{-3}$)	**Nitrate** ($\mu g\ m^{-3}$)	**Sulfate** ($\mu g\ m^{-3}$)	**Sodium** ($\mu g\ m^{-3}$)	**Iodine** ($\mu g\ m^{-3}$)
Summer Bulk[a]	5.54 ±0.192	0.0114 ±0.001	0.487 ±0.024	1.64 ±0.265	3.89 ±0.397	0.0046 ±0.0008
Winter Bulk[a]	8.63 ±0.321	0.018 ±0.0007	0.319 ±0.037	1.60 ±0.088	5.11 ±0.309	0.0080 ±0.0001
Winter Fine[a b]	2.07 ±0.240	0.0080 ±0.0006	0.0187 ±0.0197	0.552 ±0.067	1.187 ±0.234	0.0018 ±6.3e-5
Winter Coarse[a c]	6.56 ±0.211	0.0101 ±0.0004	0.300 ±0.031	1.05 ±0.056	3.92 ±0.200	0.0062 ±0.0001

Table S2: ICP-MS parameters

Laboratory & Sample Preparation	
Laboratory Name	Trace Lab, University of Washington School of Oceanography (Seattle, WA)
Sample type/mineral	Iodine in dissolved aerosols
Sample preparation	See *Sample Preparation*
ICP-MS Instrument	
Make, model, & type	iCap-RQ ICP-MS
Modes	No gas in collision/reaction cell

Sample introduction	FASTx sample introduction system with aspirating PFA nebulizer and quartz cyclonic spray chamber; no add gas used in spray chamber; standard Ni cones were used with a "high matrix" skimmer cone insert from Thermo.
RF power	1550 W
Make-up gas flow (ablation cell)	$\sim$ 1.0 L/min Ar
Reaction cell gases	He (5.0 purity) at 4.0 L/min
Masses measured	^{127}I, $^{87}Sr^{++}$, ^{103}Rh
Integration time per peak (mass)	$\sim$10 ms
Integration time per reading	0.20 s
Typical oxide rate (ThO/Th)	<2%
Data Processing	
Analytical blank	Blank filters collected during the campaign, interspersed with the sequence of sample analysis. Each daily set of size-resolved filter samples was interspersed with an 18 MΩ-cm water blank, along with rinses of the autosampler injection valve between each sample injection.
Calibration strategy	A mixture of equal contributions of dissolved iodide and iodate in 18 MΩ-cm water. Liquid concentrations of dissolved iodine ranged between 0.0009 - 0.17 μg/mL. The calibration curve contained 7 points. The errors in the slope and intercept of the calibration curve are included in the propagated error (see data availability section)
Replicate analysis	At least five replicate analyses of ^{127}iodine were performed for each sample. Replicate analyses were averaged to yield the mean concentration, and the standard deviation of the five replicates was used in the propagated error calculation
Reference material information	Potassium iodide (CAS 7681-11-0) Potassium iodate (CAS 7758-05-6)
Data processing package used	Excel

S.3 An Experimental Calibration for HOBr

Given that it is not commercially or otherwise available as a stable chemical, gaseous HOBr must be generated in real time and quantified to achieve a direct instrument calibration. Here we present results from an experimental method to produce and detect HOBr with the t-CIMS, based on previous work performed by Liao et al (2011).[70] The chemical mechanism utilized during the experiment is summarized in equations 17 through 21:

$$Br_2 + H_2O \longleftrightarrow HOBr + H^+ + Br^- \tag{17}$$

$$AgNO_3 \longrightarrow Ag^+ + {NO_3}^- \tag{18}$$

$$Ag^+ + Br^- \longrightarrow AgBr(s) \tag{19}$$

$$H^+ + {NO_3}^- \longrightarrow HNO_3 \tag{20}$$

$$HOBr + NaBr \longrightarrow Br_2 + NaOH \tag{21}$$

Shown in Figure S2 is our experimental setup involving the same permeation device and custom heater used to calibrate for Br_2 mentioned previously, the output from which is passed through a PFA three-way valve. This valve gives the option to either have the gas directly enter the t-IMR as a reference and ensure stable Br_2 signal and sensitivity (bypass), or be passed through a series of up to two chambers containing reactants involved in the mechanism above (shown in the lower path). All paths between the Br_2 permeation tube output and the t-IMR to MS interface remain free of stainless fittings, tubing, etc, as metallic surfaces were determined in previous experiments to interfere with halogenated gas transmission.

The first of the chambers is a PFA tube (with PFA swagelok fittings) containing a wetted slurry of silver nitrate, $AgNO_3$ + H_2O. This slurry acts to firstly convert Br_2 to HOBr via reaction 17, and also suppress the out-gassing of HBr and/or Br by way of reactions 18-20. The presence of silver nitrate depleting one product of reaction 17 also acts to influence the chemical equilibrium to favor the production of HOBr. The output of the $AgNO_3$ chamber (#1) is thus a gas-phase mixture of HOBr and Br_2 (as diatomic bromine is not completely reacted away), the signal of which is recorded by the t-CIMS. The second chamber is an identical tube housing which contains dry sodium bromide, NaBr. By way of reaction 21, this second chamber converts HOBr produced from chamber 1 to Br_2. The second chamber is placed in series with the first $AgNO_3$ tube and removed from the lower path multiple times as the experiment progresses to assess the reproducibility and track the evolution of the relative differences in measured signals of Br_2 and HOBr.

According to the reaction mechanism, the addition of the NaBr chamber (#2) should result in an increase

in Br_2 and a decrease in HOBr signals, while the removal of chamber 2 from the path to the IMR should show an increase in HOBr detection back to the levels of the output from chamber 1 and a decrease in bromine signal. By quantifying the absolute differences in integrated peak signal (ion counts) for both compounds, ΔHOBr and ΔBr_2, the sensitivity (C_f) ratio between the molecules can be calculated assuming that 1 molecule of HOBr (with NaBr) generates one molecule of Br_2 in the second reaction chamber:

$$\frac{C_{f,HOBr}}{C_{f,Br2}} = \frac{\Delta\text{HOBr}}{\Delta Br_2} \tag{22}$$

Shown in figure S3 for a representative experiment run is the timeseries of the measured normalized counts per million TRIC for Br_2 and HOBr iodide clusters (at m/Q 284.74 and 222.83, respectively) as well as their respective power series and polynomial fits to provide continuous tracking of the independent timeseries and reduce noise. The middle plot then shows the differences in the respective fits for signals with and without the sodium bromide chamber, i.e. ΔHOBr and ΔBr_2. And finally, the bottom plot shows the fraction of these (fitted) changes in signal, analogous to the sensitivity of HOBr relative to that of Br_2, per equation 22. Time zero reflects the point at which HOBr signal is first detected after flowing the bromine gas through the silver nitrate reaction chamber, as the wetted silver nitrate chamber takes a non-negligible amount of time to begin production and detection of ions for the $HOBrI^-$ cluster. The Br_2 signal steadily increases both with and without the addition of the NaBr reactor, which is attributed mainly to the $AgNO_3$ chamber drying over time, reducing the amount of wet surface for the fraction of Br_2 uptake to surfaces, unrelated to its detectable conversion to HOBr by the mechanism presented. Silver nitrate is added in excess at the start of the run to eliminate the possibility of being the limiting quantity and step in the reaction process. This leads to a steady increase in ΔBr_2, contrasting what is shown to be a maximum production and signal for HOBr as evidenced by ΔHOBr fit leveling off around the time of 1000 s. Shown in the bottom plot is a trace for the fraction of the relative signal changes in both compounds, which in steady-state should theoretically be constant. Steady-state is clearly not attainable for this experimental setup, and thus we take the value for $\frac{\Delta Br_2}{\Delta HOBr}$ at the time of minimum change (minimizing slope), shown in the orange data points in figure S3. After repeating the experiment, we report a range of 0.6 to 2 for the (unitless) fractional sensitivity of HOBr relative to that of Br_2, which is in reasonable agreement with the value reported by Liao et al (2011). Given that the instrument is independently and directly calibrated for Br_2, the experimental determination of the fractional sensitivities can be used to produce a value for the sensitivity of HOBr in similar conditions where $C_{f,Br2}$ is known, or in any case with known Br_2 sensitivity if one assumes this fraction to be constant.

S.4 Clean Marine Observations

In order to account for potential impacts from local activity and attempt to isolate natural atmospheric chemical processes over the remote ocean, a "clean marine" filter is applied to data. The clean marine time index is based on back trajectories calculated using the NOAA HYSPLIT model[71], where modeled air mass paths show minimal influence from Bermuda as well as the east coast of the U.S. In-situ measurements of NO_x and ozone are also used in the filter, including only data with relatively low concentrations of all three species. Shown in figure S6 are the diel cycles for the five Br^g_{y*} species detected by the t-CIMS, analogous to figure 3, filtered to include only these clean marine data points. Also shown in the sixth plot is a summary with all five median signals displayed in the same plot. The clean marine periods include over 3600 (1-minute) data points from the t-CIMS measurements, during which the winds incident on THMAO are mostly southwesterly. This index gives approximately 16% data coverage relative to the entire BLEACH23 sampling period. Each hourly bin contains at least 110 (1-minute) sample points except for 16:00 with 87 points. There is slightly more data coverage during the nighttime hours where there are over 170 data points in each bin from the hours of 18:00 - 03:00. For the clean marine periods, ozone has a mean concentration of 42 ppb with a standard deviation of (±) 5 ppb, and a maximum of 48 ppb while NO_x shows a mean concentration of 46 ± 31 ppt with a maximum of 270 ppt.

Median Br_2 observations for the clean marine period show the largest shift toward the modeled behavior based on its relatively high photolysis rate, where the enhanced concentrations during daylight hours is significantly reduced, while higher concentrations buildup after sunset (which is especially evident in the 75^{th} percentile shading). This clean marine trend reflects the current understanding of the bromine chemical mechanism where typically the strong photolysis rates during the day greatly increase Br_2 loss, outpacing gas-phase production (and/or liberation) which significantly lowers concentrations. However, there remains a slight local enhancement around 12:00 in the average, and signals are again above LOD throughout the day. This implies that there is still a somewhat significant marine source of Br_2 during the day, though it is likely either enhanced under polluted conditions (excluded from the clean marine index), or coincident with a separate local source peaking during the strongest daily photolysis rates (∼12:00-14:00 local). BrCl concentrations in the clean marine periods show a surprisingly steady trend throughout the day where median levels remain near 0.2 ppt, with a drop in signal to near zero at the hour of 9:00 shortly after sunrise recovering to the 0.2 ppt level shortly after. There is also a notable increase in the average compared to the unfiltered data around sunset between the hours of 18:00-19:00.

The diel shape for HOBr remains approximately the same as the unfiltered profile, with a slightly larger and later peak median concentration around midday, which subsequently returns to near or below background

after the cessation of active photochemistry. BrO remains near detection limits in the average, with no noticeable enhancement during the day, contrary to the slight increase evident in the campaign-long trend. This is indicative that BrO reactivity remains relatively high in the clean marine MBL, where its loss reactions occur on pace or faster than it's formation. Importantly for this clean marine period, the diurnal cycle for $BrONO_2$ shows what is essentially a complete loss of signal, where the median for each hourly bin is 0 with even the 75^{th} percentile of concentrations at or below the LOD at almost all hours. This indicates what is likely a significant shift in the fate of BrO away from the bromine nitrate production pathway, caused by very low concentrations of NO_2 relative to the rest of the observations. This aligns with the results presented in figure 4, suggesting the existence of a minimum NO_2 or NO_x threshold for formation and detectable (above single ppq) levels of bromine nitrate. These clean marine daily cycles along with the wind rose analysis discussed previously present observational evidence for an effect of anthropogenic activity and a generally more polluted environment on the reactive bromine cycle in the marine atmosphere.

S.5 Constraining Heterogeneous Uptake Coefficients

The rate at which heterogeneous reactions occur is dependent on both the gas-phase diffusivity and probability of reaction given a collision of the gas-phase species with the aerosol particle. The unitless reactive uptake coefficient for a given molecule, γ, is defined as the ratio of the number of reactive collisions divided by the total number of gas-particle collisions, ranging from 0 (no reactivity) to 1 (every gas-particle collision results in reaction). Uptake to and reaction on aerosols has been assumed to be the rate-limiting step for the heterogeneous cycling of halogens in the marine atmosphere.[72]

The uptake of HOBr onto NaCl particles has been the subject of multiple laboratory studies, and thought to be one of the most important reactions driving the debromination of SSAs, yet the magnitude of its uptake (γ_{HOBr}) remains highly uncertain, along with γ_{BrONO2}. γ_{HOBr} has been demonstrated to be dependent on ambient RH, as well as the size and pH of aerosol particles. Heterogeneous reactivity for HOBr is generally higher for slightly acidic particles compared to alkaline. Though on highly acidified fine particles, particulate bromide has shown enhancements, implying a nonlinear relationship with heterogeneous cycling and pH.[73] Pratt and Rossi (2006) found that, at least for aerosols less than 1 μm in size, that increasing particle diameter increases γ. Longer interaction times for gases in larger volume particulates is attributed in part to the increased reactive uptake, while higher RH also is associated with fast depletion of HOBr in the presence of salt particles.[74] SSA acidified by sulfate typically results in Cl^- depleted aerosol, causing the uptake of reactive halogens (e.g. HOBr and $BrONO_2$) to become more dependent on available Br^- (and to a lesser extent, I^-). Ozone concentrations have also been reported to modulate heterogeneous reactivity within the

bromine cycle. In low ozone (O_3-limited) regimes, production of Br_2 stems mostly from gas phase reactions, e.g. the self-reaction of BrO, while Br_2 concentrations demonstrate a higher sensitivity to heterogeneous chemistry in ozone-rich environments (a Br-limited case).[75]

The theoretical heterogeneous reactive uptake rate, k_{het}, of gaseous molecule X onto aerosol surfaces is dependent on the properties of both the gas-phase molecule and size distribution of aerosol:[76]

$$k_{het}^X = (\frac{r}{D_g^X} + \frac{4}{v_X \gamma_X})^{-1} A \tag{23}$$

where D_g^X is the gas phase diffusivity ($cm^2\ s^{-1}$), v_X is the mean molecular speed ($cm\ s^{-1}$), and γ_x is the reactive uptake coefficient (unitless) for gas phase compound X. Meanwhile r represents the aerosol average particle radius (cm) and A the surface area concentration ($cm^2\ cm^{-3}$). Gas phase diffusivities for the molecules HOBr and $BrONO_2$ are estimated using the method set by Tang et al using the sum diffusion volume of each atomic component in N_2.[77] Mean molecular speeds are calculated for each species based on their respective molar mass (M_X), along with ambient temperature (T, in Kelvin) measurements taken on site according to the equation:

$$v_X = \frac{8 k_B T\ n_A}{\pi M_X} \tag{24}$$

where k_B is the Boltzmann constant, $1.380649 \cdot 10^{-23}\ J\ K^{-1}$ and n_A is Avogadro's number, $6.0221 \cdot 10^{23}$. While aerosol filter measurements were conducted for the BLEACH campaign, particle sizing instrumentation was not present at the site, leaving a gap in observational data for both particle radius and aerosol area concentration. However, if the ratio of k_{het} is taken for two molecules, the area concentration (A) and the need of such a measurement is eliminated in the calculation (equation 23), given that both gaseous species are assumed to be well mixed and interacting with the same aerosol distribution. This leaves only the average particle radius to be prescribed when analyzing the effect of reactive uptake coefficients (γ) on the ratio of uptake rates.

Figure S7 displays this effect in the form of the uptake coefficient for $BrONO_2$ vs. that of HOBr, where the contour lines (increasing in value from green to blue color) display the resulting ratio of $\frac{k_{het}^{HOBr}}{k_{het}^{BrONO2}}$ according to equation 23. For this analysis, an average particle radius of 1 μm (10^{-4} cm) is prescribed based on the mean modeled output for wet SSA radius from the GEOS-Chem simulation. As mentioned previously, the uptake coefficients are unitless quantities between values 0 and 1 for any gas phase compound, where 0 indicates that the molecule never undergoes reaction on aerosol surfaces and a value of 1 would mean that there is always a reaction when the species collides with the surface of a particle, implying that the reaction would be limited only by the collision rate of the gas molecule and particles. These quantities are important for

models as they affect the speed at which heterogeneous uptake and subsequently gas-phase recycling (in this case for halogens) is represented. Evident in the plot is the organization of the contours as the uptake rate ratio becomes much smaller or larger. As the value approaches zero, one can see that the contours, e.g. the green at a k_{het} ratio of 0.01, become nearly vertical along the y-axis. If this were the true value, it would put a relatively small upper limit on γ_{HOBr}, while leaving γ_{BrONO2} almost completely unconstrained, meaning that nearly any value of γ_{BrONO2} between 0 and 1 would be possible and result in the given uptake rate ratio. Conversely as $\frac{k_{het}^{HOBr}}{k_{het}^{BrONO2}}$ increases, e.g. the blue contour ratio of 3, shows the opposite, where γ_{BrONO2} would be constrained with a small upper limit while γ_{HOBr} remains unbounded.

In an effort to constrain the uptake coefficients for HOBr and $BrONO_2$, $\frac{k_{het}^{HOBr}}{k_{het}^{BrONO2}}$ is estimated independently using an alternative theoretical relationship where we include the gas-phase Br_{y*}^{g} measurements made by the t-CIMS in the MBL. This is accomplished by accounting for total production and loss for the two gases, and assuming steady state for a chosen sampling period. We apply a generalized total heterogeneous loss term for both species using their heterogeneous reactive uptake rates: $L_{het}^{X} = k_{het}^{X}[X]$ and assume that heterogeneous loss and photolysis are much larger than loss due to deposition. Using only this heterogeneous loss term, gas phase reactions, and photolysis, we approximate the total production and loss for both compounds to calculate the change in concentration over time ($d[X]/dt$):

$$\frac{d[HOBr]}{dt} = k_{BrO,HO2}[\mathrm{BrO}][\mathrm{HO_2}] - (j_{HOBr} + k_{het}^{HOBr})[\mathrm{HOBr}] \tag{25}$$

$$\frac{d[BrONO2]}{dt} = k_{BrO,NO2}[\mathrm{BrO}][\mathrm{NO_2}] - (j_{BrONO2} + k_{het}^{BrONO2})[\mathrm{BrONO_2}] \tag{26}$$

Where $k_{X,Y}$ represents corresponding gas-phase reaction rates for species X and Y, and j_X is the photolysis rate. Assuming steady state for both compounds, $d[X]/dt$ becomes zero in each equation, which can then be rearranged to solve for k_{het}^{X}. The ratio of the reactive uptake rates can then be calculated resulting in the following steady-state relationship:

$$k_{het}\ \mathrm{HOBr} : \mathrm{BrONO_2} \equiv \frac{k_{het}^{HOBr}}{k_{het}^{BrONO2}} = \frac{\frac{k_{BrOHO2}[\mathrm{BrO}][\mathrm{HO_2}]}{[\mathrm{HOBr}]} - j_{HOBr}}{\frac{k_{BrONO2}[\mathrm{BrO}][\mathrm{NO_2}]}{[\mathrm{BrONO_2}]} - j_{BrONO2}} \tag{27}$$

Between the t-CIMS, LIF, and spectral radiometer instruments, we have coordinated observations during BLEACH23 for all variables in equation 27, other than the gas-phase reaction rates and $[\mathrm{HO_2}]$. Values for k_{BrOHO2} and k_{BrONO2} (corresponding to gas-phase reaction rates of BrO with HO_2 and NO_2, respectively), are calculated using the temperature-dependent equations published in the JPL Chemical Kinetics Evaluation number 17.[30] HO_2 concentrations are estimated and prescribed using observations from Elshorbany et al

(2022), reaching a maximum of 23 ppt during midday (14:00 local time) and a minimum of less than 0.01 ppt around 06:00.[46]

The concentrations of BrO, HOBr, and $BrONO_2$ as measured by the t-CIMS in ppt are converted to units of molecules cm^{-3} using temperature and pressure data from THMAO. Data is filtered to include only points where these three compounds were simultaneously measured above their respective detection limits and during daylight hours to account for only the photolytically driven processes. For the steady-state assumption leading to equation 27 to be valid, the concentrations of HOBr and $BrONO_2$ must remain unchanged in time. To satisfy this requirement as closely as possible, a period of time between 14:30 and 16:00 on Jan 25th 2023 is chosen, where the average concentrations and standard deviation for HOBr is 0.64 $\pm$ 0.15 ppt and that for $BrONO_2$ is 0.42 $\pm$ 0.14 ppt. The number of 1-minute data points in this period which survive the preceding indexing filters is 36. The resulting average of $k_{het}HOBr : BrONO2$ is 0.05 with a standard deviation of 0.04. Using this value in the context of figure S7, an upper limit on the uptake coefficient for HOBr can be defined via equation 23, and visually by following the contour for the upper estimate of $k_{het}HOBr : BrONO2$ at 0.1 to it's maximum value along the x-axis ($\gamma_{BrONO2} = 1$). This steady-state analysis thus suggests an upper limit for γ_{HOBr} at a value of 0.015. This analysis represents a single point and location of observation for such a limit with multiple assumptions, but is meant to provide observational evidence for constraining the uptake rates utilized in model studies of the bromine chemical mechanism. It also falls into the previously described scenario where a small upper limit is placed on γ_{HOBr}, while γ_{BrONO2} remains essentially completely unconstrained between 0 and 1, suggesting that the reactive uptake of HOBr may be much lower than that of $BrONO_2$ for our sampling conditions.

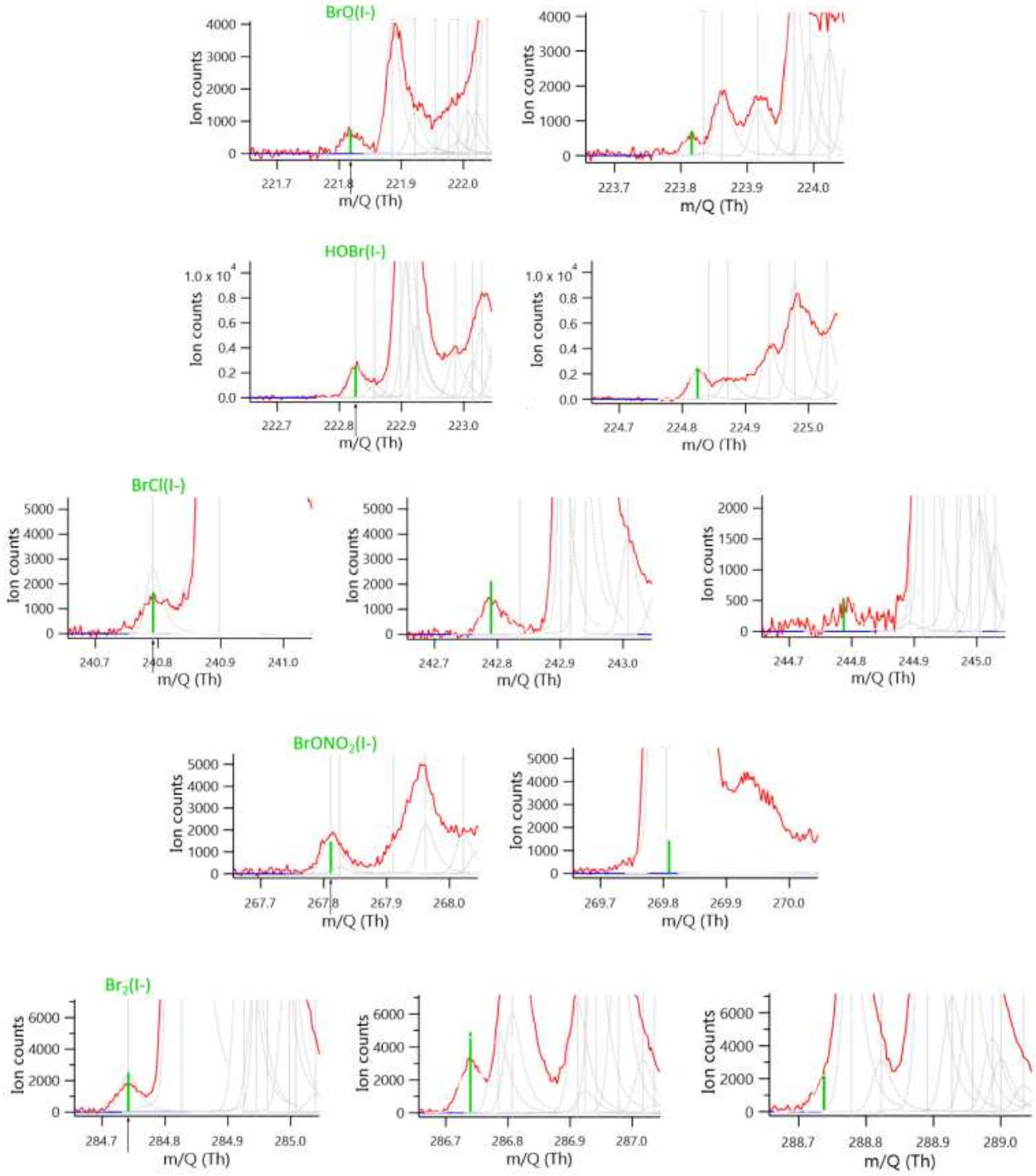

Figure S1: Representative t-CIMS spectra showing peak identification for five bromine-containing species and their isotopes when clustered with I^-. Red traces represent raw spectra (binned ion counts) as measured, while green bars with labels show exact mass-to-charge positions and fitted heights for the peak centers of each compound. Corresponding isotope peaks are shown to the right of each compound.

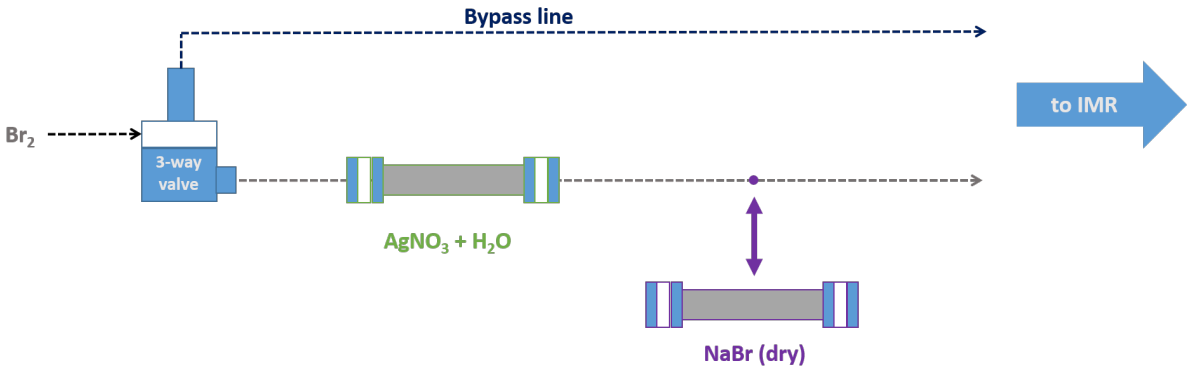

Figure S2: Simplified setup for t-CIMS calibration of HOBr. Br_2 gas is passed through a 3-way valve and then either directly to the Transverse IMR (Bypass line, top path) or through a silver nitrate ($AgNO_3$) slurry solution and a removable bed of dry sodium bromide (NaBr) crystals (bottom path).

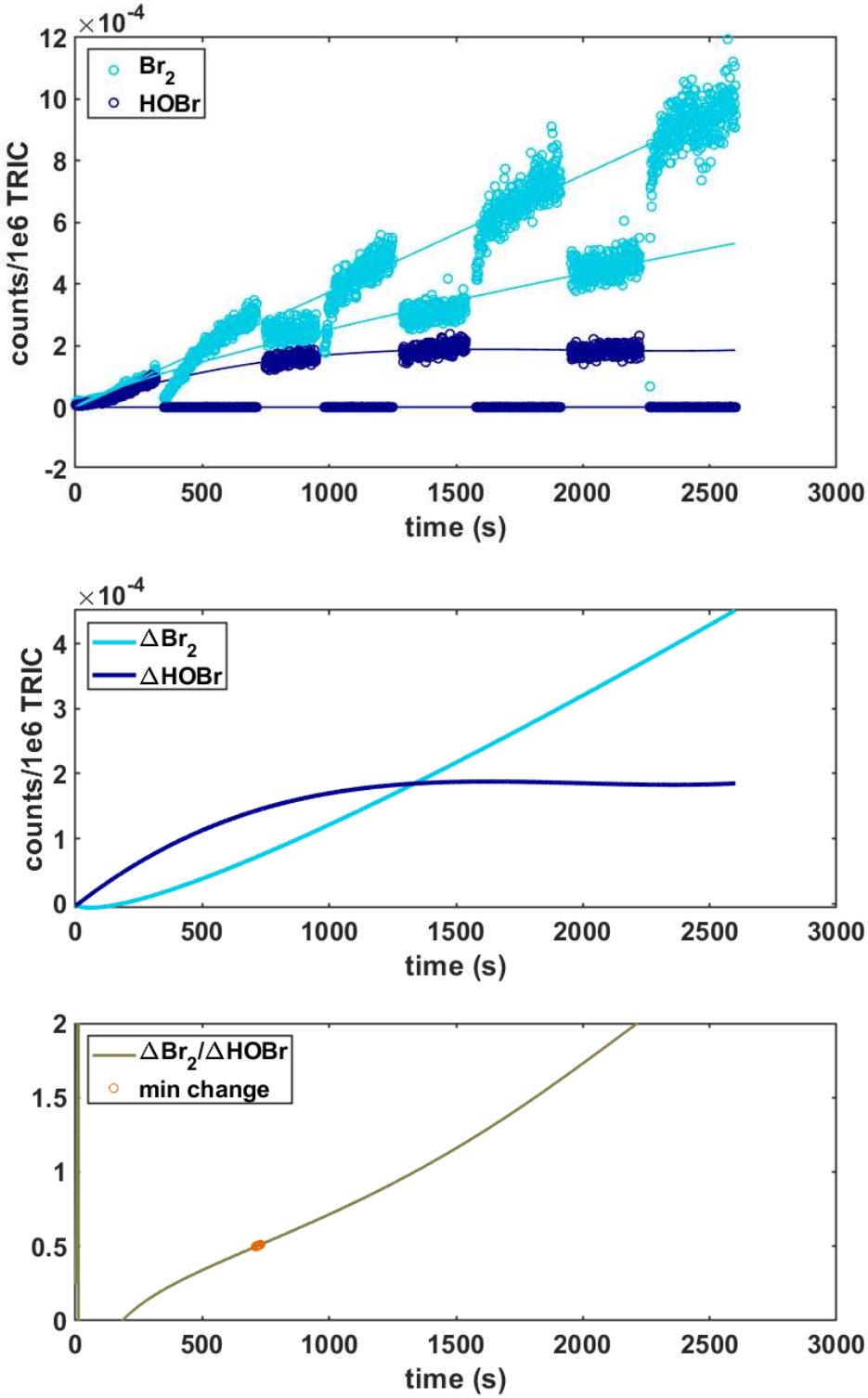

Figure S3: [Top] Timeseries of measured signals (circles) in normalized counts per 1 million TRIC for Br_2 (light blue) and HOBr (navy) iodide clusters, along with power series and polynomial fits (solid lines). [Middle] Absolute difference in measured signal fits with and without the addition of NaBr chamber. [Bottom] Fraction of changes in signal traced through experiment (brown solid line), and the values at minimum slope (orange circles).

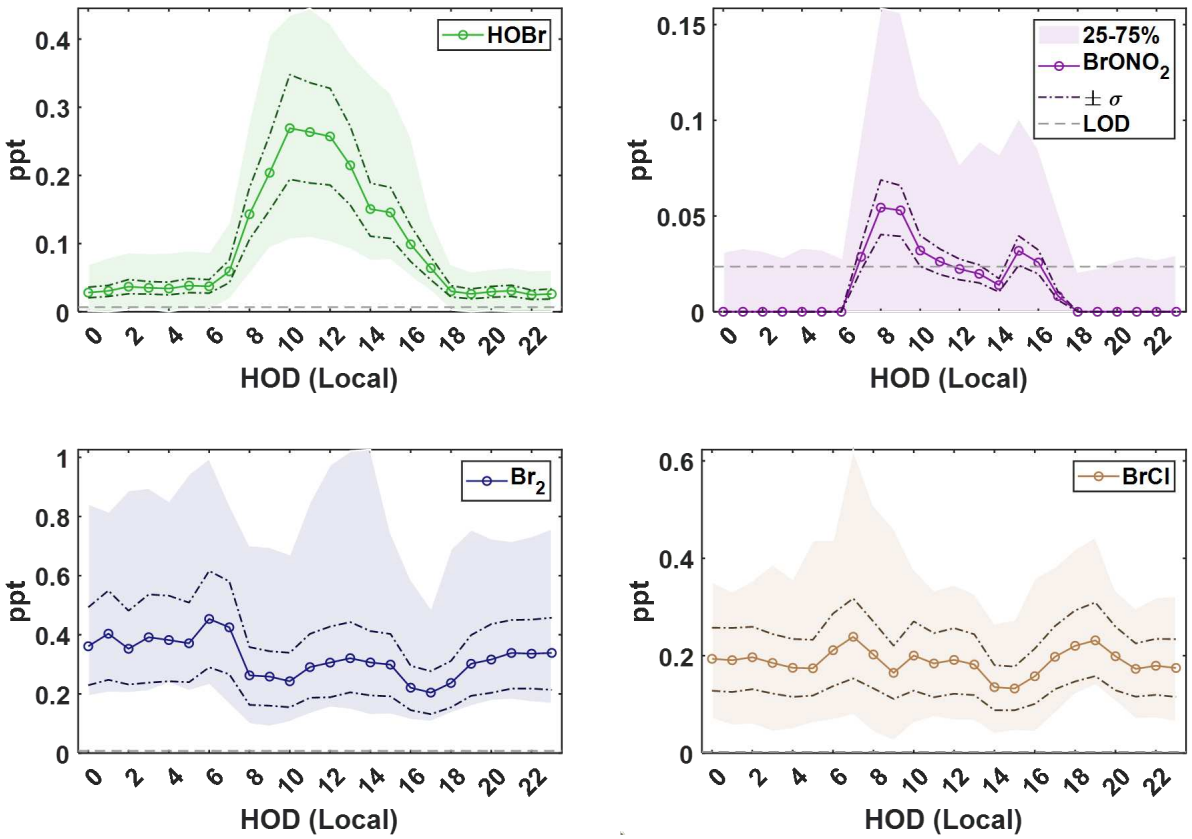

Figure S4: Diurnal profiles o HOBr, $BrONO_2$, Br_2, and BrCl as measured by the t-CIMS at THMAO during the BLEACH23 campaign, including all viable data (with offshore winds and local island influence). Open circle traces show the median concentration for the given compound at each hour of the day for all included points, shading represents the 25^{th} to 75^{th} percentile concentrations, and the darker color dot-dashed traces show the median $\pm 1\sigma$ of propagated uncertainty in concentration. Dashed gray lines indicate the respective limits of detection (LOD) for each.

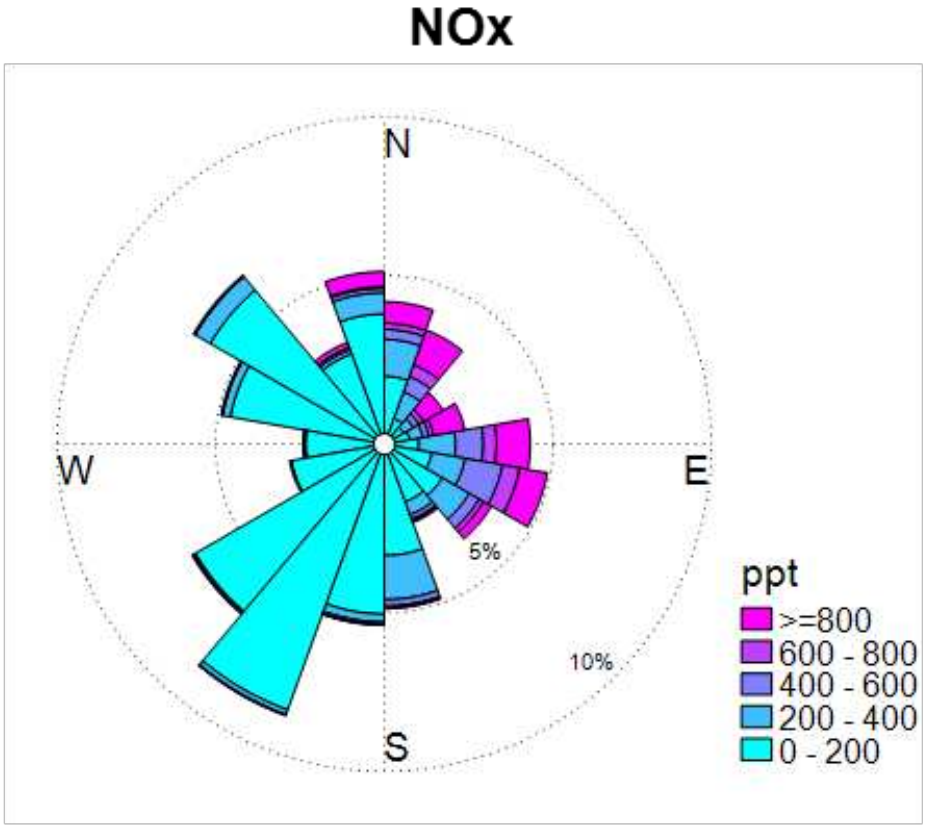

Figure S5: Wind rose of NO_x concentrations, analogous to figure 2. Here, magenta colors show higher concentrations while cyan represent lower. Wedge size still corresponds to measurement frequency.

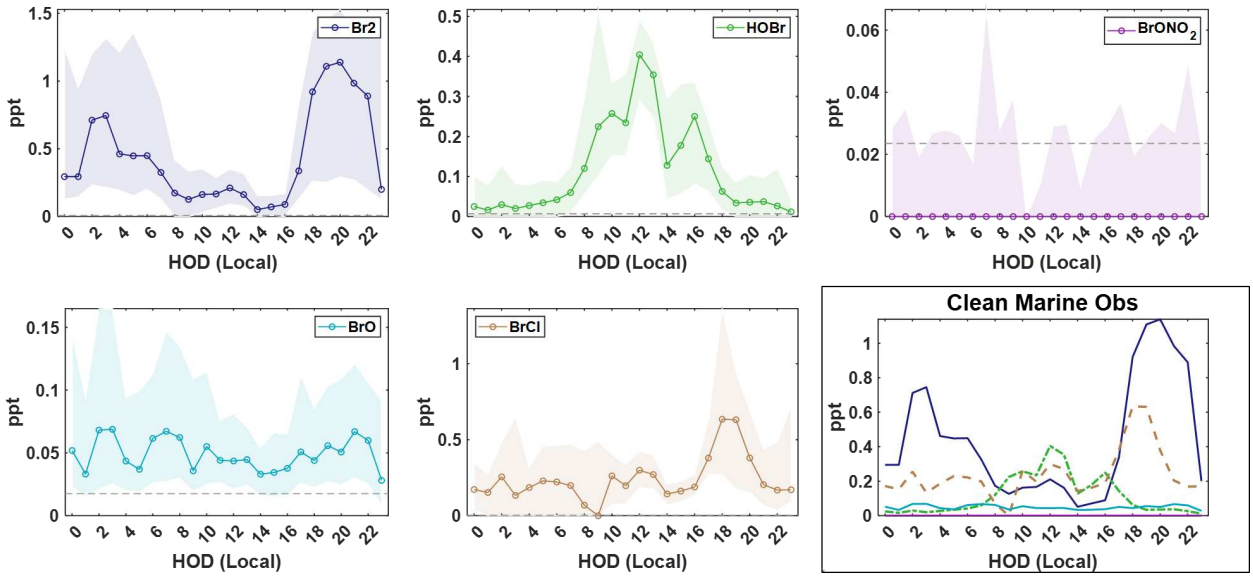

Figure S6: Individual diurnal profiles of observed Br_y species during the BLEACH winter leg, filtered to include only data designated as "clean marine-sourced" based on backtrajectory analysis, wind direction, NO_x and O_3 levels. Each plot shows a given compound's median concentration in ppt for each (local) hourly bin and shading to show the 25^{th} to 75^{th} percentiles, and gray dashed traces to indicate the LOD for a given species, with the exception of the bottom right plot which summarizes the median diel cycles for all five species. Br_2 is shown in dark blue, HOBr in green dashes, $BrONO_2$ in purple, BrCl in brown dashes, and BrO in light blue.

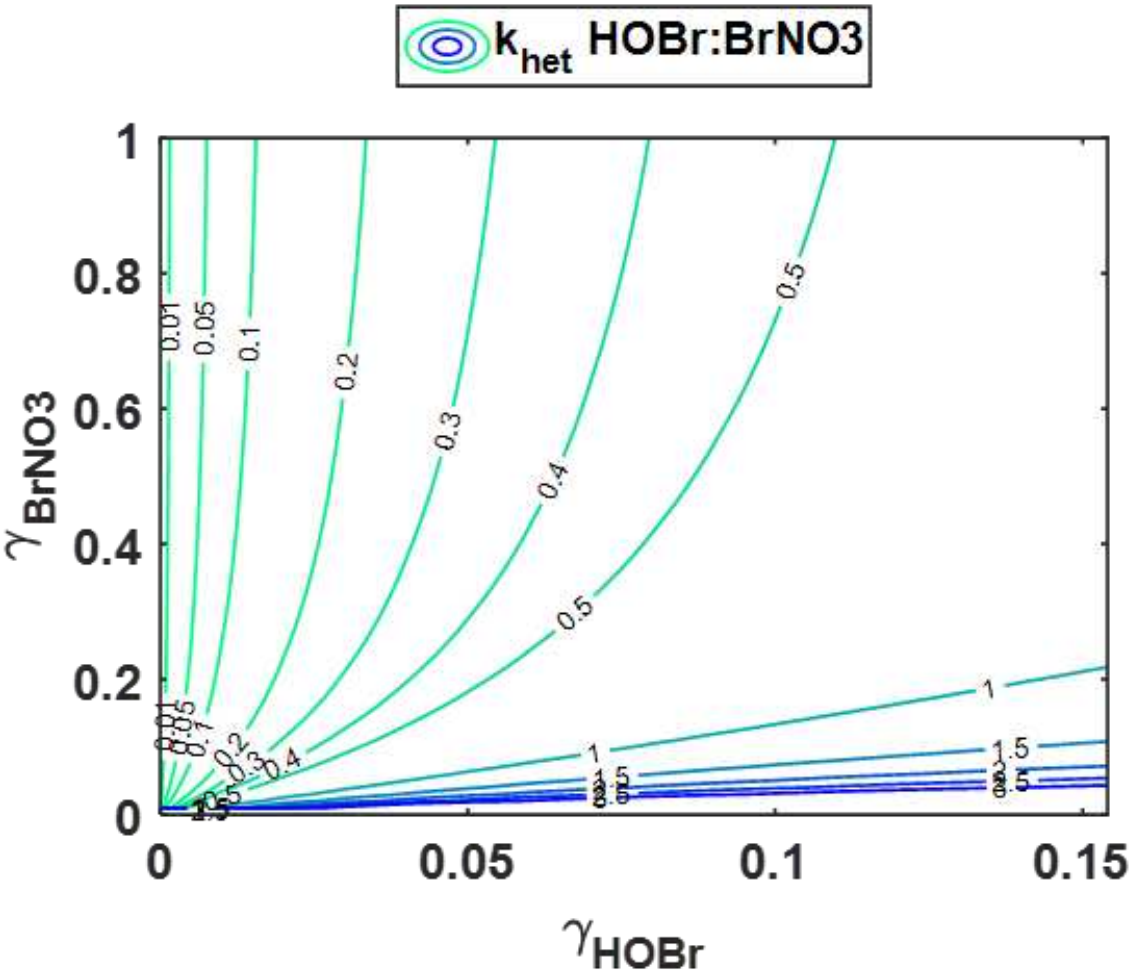

Figure S7: Contour plot showing the ratio of heterogeneous uptake reaction rates (k_{het}) for HOBr relative to that of $BrONO_2$. Reactive uptake coefficients (γ) for gaseous HOBr and $BrONO_2$ onto aerosol surfaces are shown on the x and y axes, respectively.

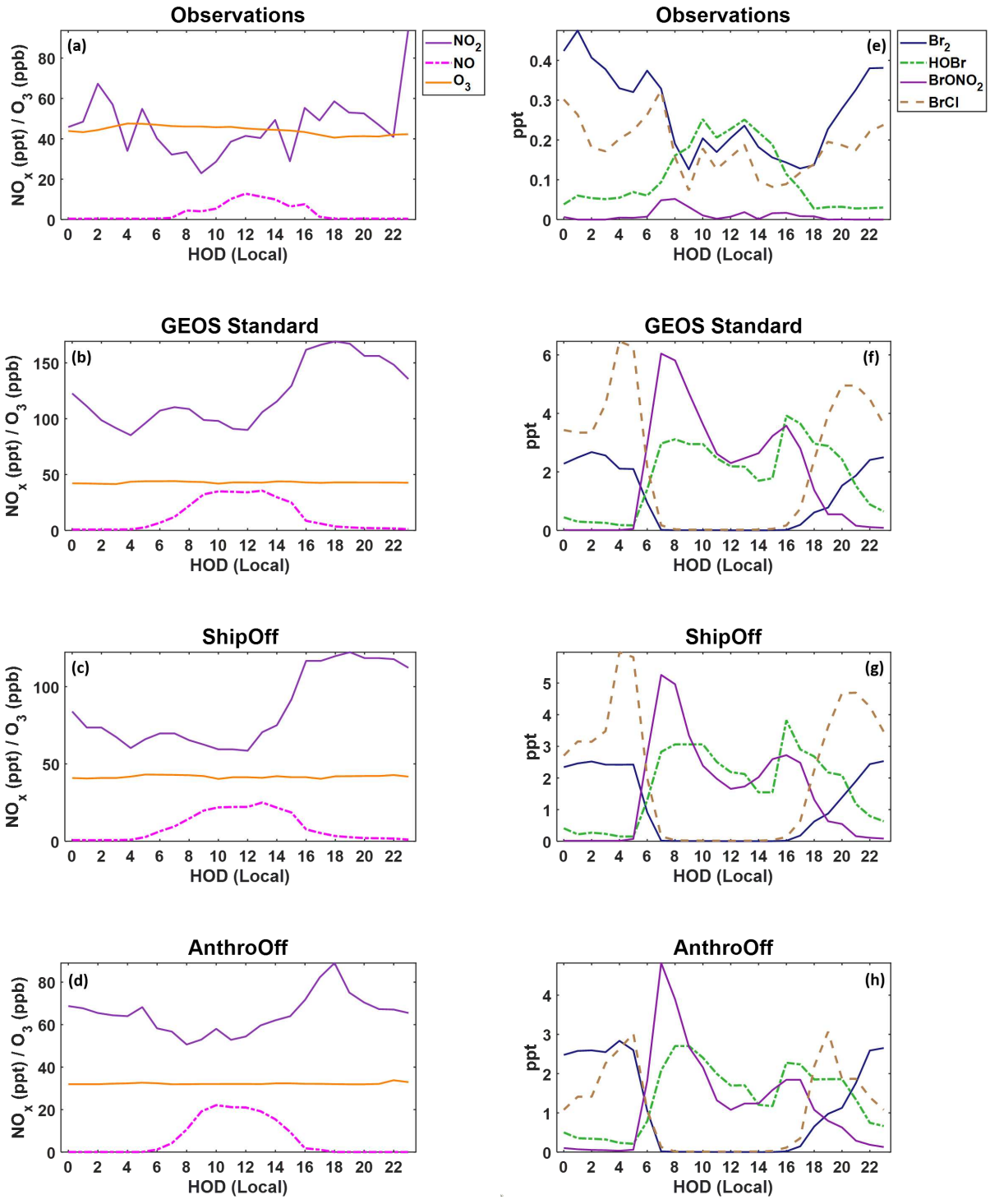

Figure S8: Panels (a)-(d): Diurnal profiles of NO_x and O_3 from BLEACH23 observations, as well as three GEOS-Chem model simulations: standard, ShipOff (no ship emissions), and AnthroOff (no anthropogenic emissions). Panels (e)-(f): Diurnal profiles from BLEACH23 and model simulations for Br_{y*}^{g} species.

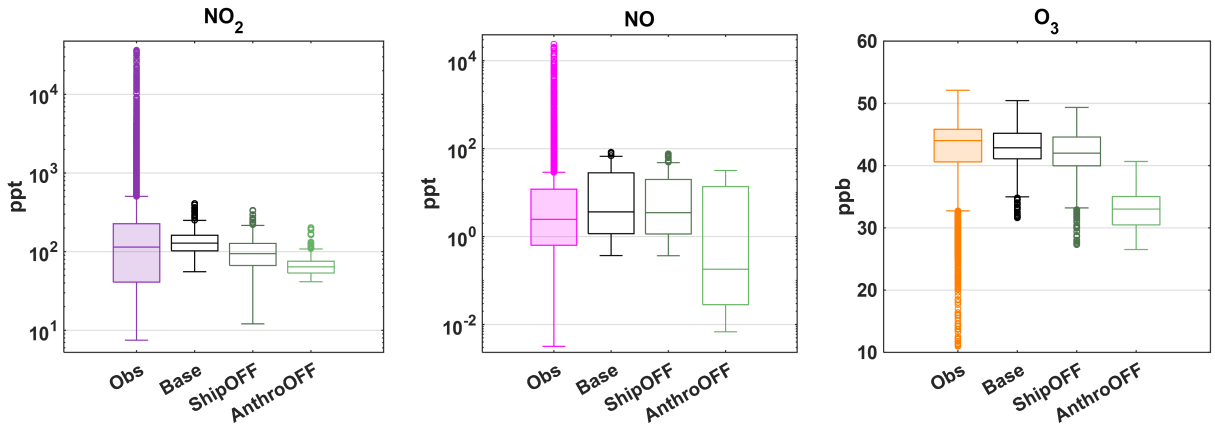

Figure S9: Box chart distributions of NO_x in ppt on a log scale and O_3 in ppb from BLEACH23 observations (Obs, shaded boxes), as well as from three GEOS-Chem model simulations: standard (Base, black), ShipOff (dark green), and AnthroOff (light green).

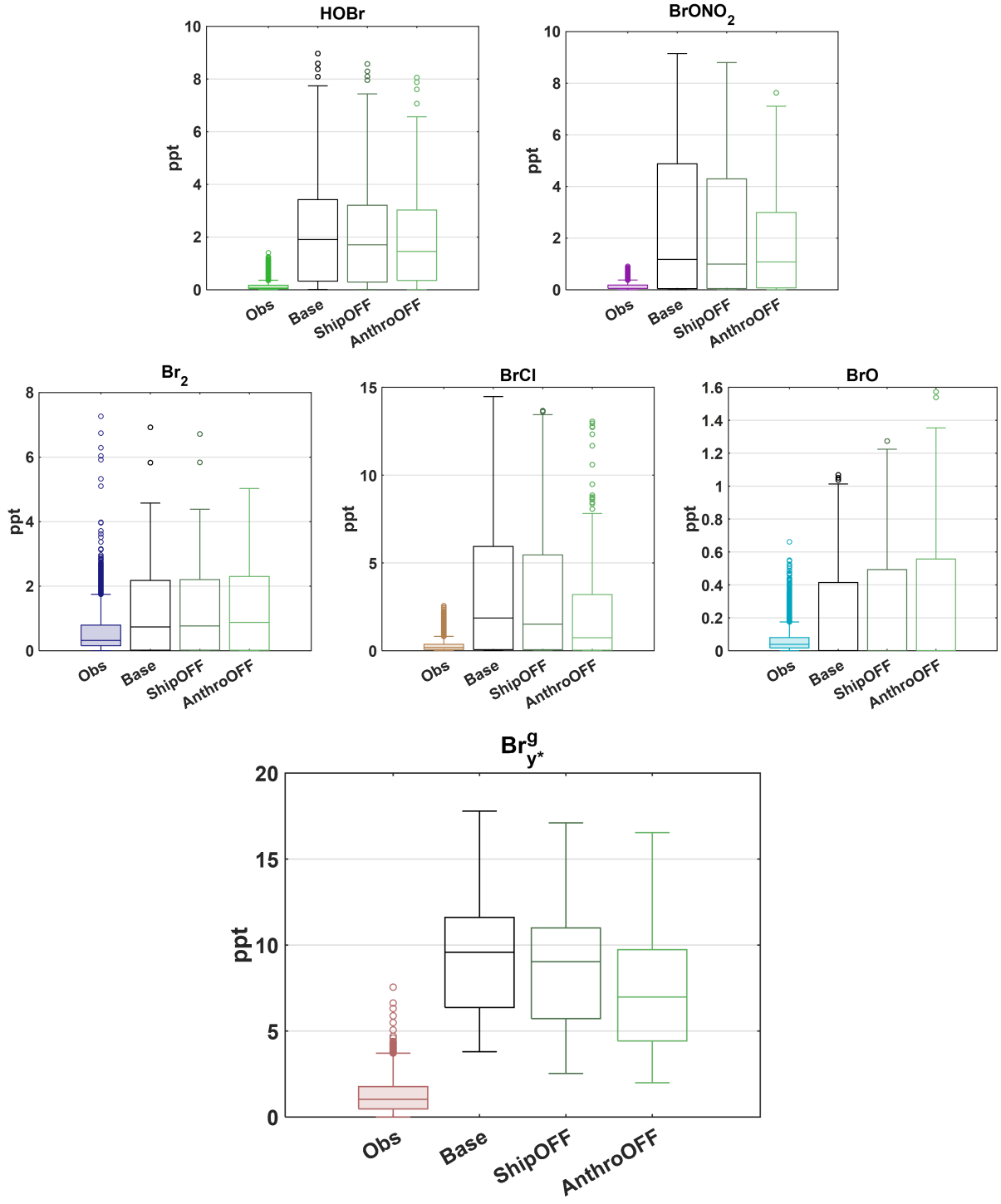

Figure S10: Same as figure S9 but for total Br^{g}_{y*} and its constituents. Concentrations reported in ppt.

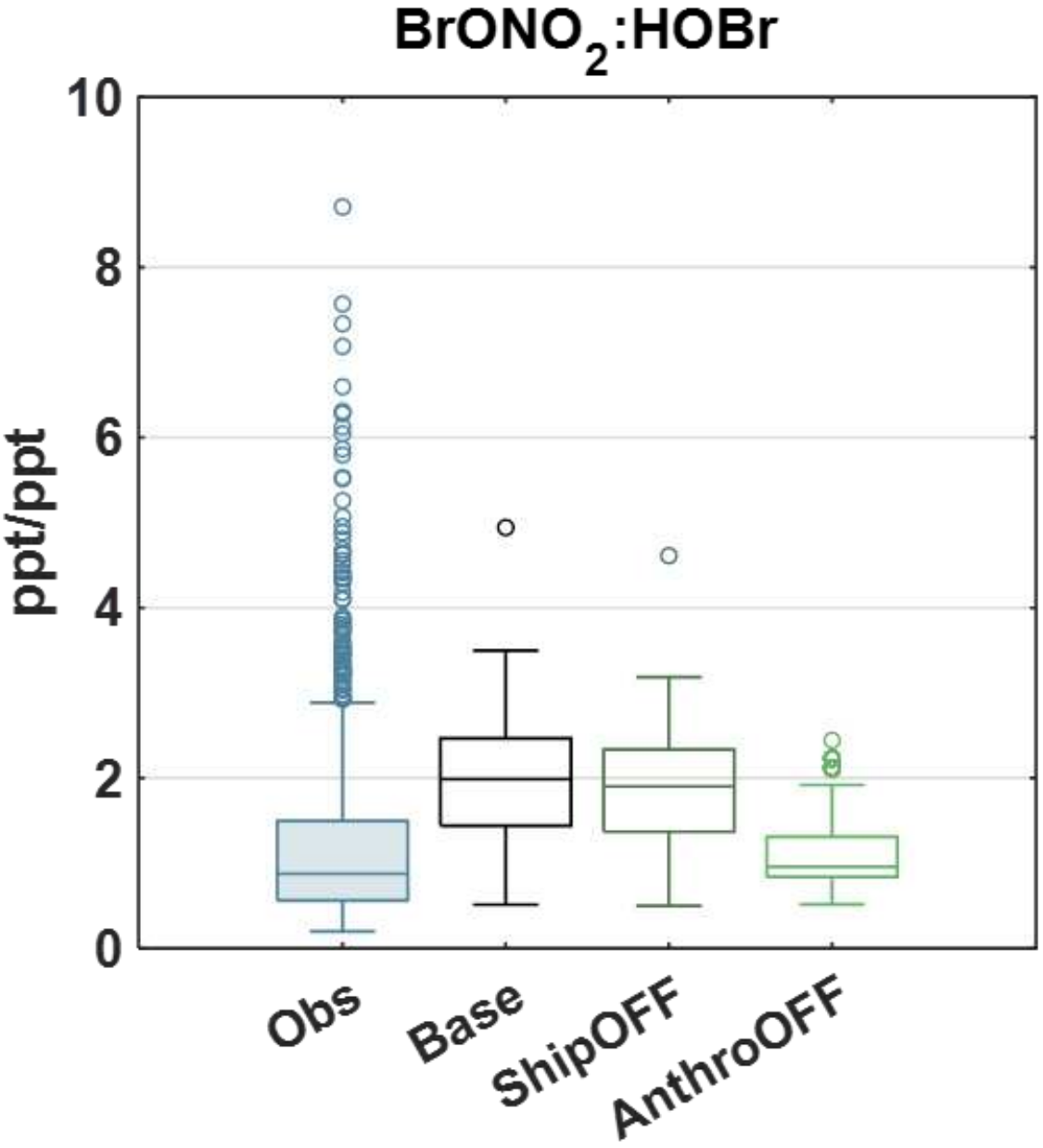

Figure S11: Same as figure S9 but for the ratio of $BrONO_2$:HOBr concentrations (in ppt/ppt). Data is filtered to only include concentrations when both compounds were detected above LOD and during daylight hours.